

## HEATING THE IGM BY X-RAYS FROM POPULATION III BINARIES IN HIGH REDSHIFT GALAXIES

HAO XU<sup>1</sup>, KYUNGJIN AHN<sup>2</sup>, JOHN H. WISE<sup>3</sup>, MICHAEL L. NORMAN<sup>1</sup>, AND BRIAN W. O'SHEA<sup>4</sup>

*Draft version August 6, 2018*

### ABSTRACT

Due to their long mean free path, X-rays are expected to have an important impact on cosmic reionization by heating and ionizing the intergalactic medium (IGM) on large scales, especially after simulations have suggested that Population III (Pop III) stars may form in pairs at redshifts as high as 20 - 30. We use the Pop III distribution and evolution from a self-consistent cosmological radiation hydrodynamic simulation of the formation of the first galaxies and a simple Pop III X-ray binary model to estimate their X-ray output in a high-density region larger than 100 comoving (Mpc)<sup>3</sup>. We then combine three different methods — ray tracing, a one-zone model, and X-ray background modeling — to investigate the X-ray propagation, intensity distribution, and long-term effects on the IGM thermal and ionization state. The efficiency and morphology of photoheating and photoionization are dependent on the photon energies. The sub-keV X-rays only impact the IGM near the sources, while the keV photons contribute significantly to the X-ray background and heat and ionize the IGM smoothly. The X-rays just below 1 keV are most efficient in heating and ionizing the IGM. We find that the IGM might be heated to over 100 K by  $z = 10$  and the high-density source region might reach  $10^4$  K, limited by atomic hydrogen cooling. This may be important for predicting the 21 cm neutral hydrogen signals. On the other hand, the free electrons from X-ray ionizations are not enough to contribute significantly to the optical depth of the cosmic microwave background to the Thomson scattering.

*Keywords:* cosmology:theory – methods: numerical – hydrodynamics – radiative transfer – galaxy:high-redshift – X-rays:galaxies – dark ages, reionization, first stars

### 1. INTRODUCTION

The appearance of the first luminous objects marks the end of the cosmic dark ages after recombination and the beginning of the last cosmic phase transition of reionization. Subsequently, the universe begins to be heated and ionized by radiation from first stars and galaxies and their descendants. Physical processes of the heating and ionization before the universe fully ionized at  $z \sim 6$  are still not completely understood. It is one of the most important problems in astrophysics and cosmology in both theory and observation to obtain the thermal and ionization histories of the universe during this transition period.

The first generation stars, Population III (Pop III), form from metal-free gas in dark matter halos with  $M \gtrsim 10^6 M_\odot$  and have a large characteristic mass (e.g., Abel et al. 2002; Bromm et al. 2002; O'Shea & Norman 2007; Turk et al. 2009; Greif et al. 2012). Due to their high mass, they have short lifetimes (Schaerer 2002), may go supernova (SN; e.g., Heger et al. 2003), and enrich their surrounding intergalactic medium (IGM). Once the metallicity of the star-forming gas passes some critical metallicity,  $\sim 10^{-6} Z_\odot$  if dust cool-

ing is efficient (Omukai et al. 2005; Schneider et al. 2006; Schneider & Omukai 2010; Omukai et al. 2010; Dopcke et al. 2013) or  $\sim 10^{-3.5} Z_\odot$  otherwise (Omukai 2000; Bromm et al. 2001; Smith et al. 2009; Meece et al. 2014), the gas can cool rapidly and lower its Jeans mass. These metal-enriched Population II (Pop II) stars have a lower characteristic mass scale and most likely have an initial mass function (IMF) that resembles the present-day one.

Pop III stars can self-regulate their formation through chemical and radiative feedback. The transition from Pop III to Pop II star formation and the end of the massive Pop III formation are strongly dependent on the metal enrichment from the Pop III SN remnants in the future star-forming halos. Metal enrichment involves complex interactions between SNe blastwaves, the IGM, halo mergers, and cosmological accretion. This topic has been extensively studied with semi-analytic models (Scannapieco et al. 2003; Yoshida et al. 2004; Tumlinson 2006; Salvadori et al. 2007; Komiya et al. 2010; Gómez et al. 2012; Crosby et al. 2013a), post-processing of numerical simulations (Karlsson et al. 2008; Trenti et al. 2009), and direct numerical simulations (Tornatore et al. 2007; Ricotti et al. 2008; Maio et al. 2010; Wise et al. 2012b; Muratov et al. 2013b; Xu et al. 2013). Studies have suggested that Pop III stars may continue to form at low redshifts to the end of reionization. For example, Trenti et al. (2009) suggested that Pop III stars may still form at the late epoch of  $z = 6$  in the under dense regions of the universe by post-processing of cosmological simulations with blast wave models. Muratov et al. (2013b) also showed that Pop III stars continue to form until  $z = 6$  using direct

<sup>1</sup> Center for Astrophysics and Space Sciences, University of California, San Diego, 9500 Gilman Drive, La Jolla, CA 92093; hxu@ucsd.edu, mlnorman@ucsd.edu

<sup>2</sup> Department of Earth Science Education, Chosun University, Gwangju 501-759, Korea; kjahn@chosun.ac.kr

<sup>3</sup> Center for Relativistic Astrophysics, School of Physics, Georgia Institute of Technology, 837 State Street, Atlanta, GA 30332; jwise@gatech.edu

<sup>4</sup> Lyman Briggs College and Department of Physics and Astronomy, Michigan State University, East Lansing, MI 48824; oshea@msu.edu

cosmological simulations.

Pop III star formation is also regulated by the Lyman-Werner (LW) radiation between 11.2 and 13.6 eV that is mostly produced by Pop III and II stars. LW photons photodissociate  $H_2$  by the Solomon process and then suppress the formation of Pop III stars in low-mass halos (Machacek et al. 2001; Yoshida et al. 2003; Wise & Abel 2007; O’Shea & Norman 2008). Though LW radiation will not completely suppress Pop III formation, it delays the formation of Pop III stars by increasing the mass of Pop III forming halos (O’Shea & Norman 2008; Xu et al. 2013), which has complicated consequences on the later star formation of both Pop II and Pop III by changing the metal enrichment and radiation feedback. For example, whether or not the enriched gas can be ejected from the host halo is dependent on the halo masses (Whalen et al. 2008a; Muratov et al. 2013a). In addition, since LW photons have long mean free paths in the neutral IGM, LW radiation has a significant impact on Pop III formation in distant halos ( $\sim 100$  comoving Mpc) and usually needs to be handled carefully (e.g. Haiman et al. 2000; Wise & Abel 2005; Ahn et al. 2009).

Because Pop III star formation is easily impacted by the environment due to chemical and radiative feedback from nearby star-forming halos, it is necessary to follow both the Pop II and Pop III formation and feedback during early galaxy formation over a large cosmic volume to track their interaction between star-forming halos. In Xu et al. (2013), we performed a self-consistent cosmological radiation hydrodynamics simulation of Pop III and Pop II formation and feedback in a volume larger than 100 comoving  $Mpc^3$ . This cosmological simulation includes a full primordial chemistry network, radiative cooling from metal species, models for both Pop II and Pop III star formation and their radiative, mechanical, and chemical feedback, allowing us to obtain a complete formation history of Pop III stars in a statistically complete volume of  $\sim 140$  comoving  $Mpc^3$ , in which over 13,000 Pop III stars form.

In addition to the metal enrichment and LW radiation from Pop III stars, heating and ionizing effects from their radiation in other bands are crucial to modeling early structure formation of the universe (Gnedin & Ostriker 1997; Gnedin 2000; Haiman et al. 2000). The Lyman continuum radiation from Pop III stars then affects the subsequent structure formation through heating and ionizing the surrounding IGM (Machacek et al. 2001; Yoshida et al. 2003; Wise & Abel 2008; O’Shea & Norman 2008). The effects of this ionizing UV radiation from stellar sources on the first galaxies are well studied (Ricotti et al. 2002a,b; Wise & Abel 2008; Greif et al. 2010; Wise et al. 2012a,b; Muratov et al. 2013a). However, the global impact of UV radiation from Pop III stars on IGM is currently under debate. While it is agreed that Pop III stars cannot finish reionization alone, they may contribute significantly by ionizing the universe up to  $\sim 20\%$  (e.g., Haiman & Bryan 2006; Ahn et al. 2012) or may be negligible (e.g., Sobacchi & Mesinger 2013) due to negative radiative and mechanical feedback effects (e.g., O’Shea & Norman 2008; Whalen et al. 2008b; Tseliakhovich & Hirata 2010). This question has been addressed more self-consistently than before by simulations in a large ( $> \sim 100$  Mpc) box (to incorporate

large-scale radiative feedback) with embedded subgrid microphysics on Pop III star formation (Ahn et al. 2012; Fialkov et al. 2013), but a conclusive answer is yet to come with even more self-consistent treatment of both global and local feedback effects. X-ray radiation from Pop III (stars or remnants) might also serve as a significant source of heating and ionization of the IGM during reionization, mainly due to its high efficiency in penetrating the IGM with much longer mean free path than UV radiation and thus generating global X-ray background.

Simple vanilla models of reionization predict Thomson scattering optical depth of the cosmic microwave background (CMB), which usually differs a lot from the observed value. While the observation by Planck is  $\tau_e = 0.089 \pm 0.032$  (Planck Collaboration et al. 2013), instantaneous ionization produces  $\tau_e \sim 0.048$  if it occurs at  $z \sim 7$ , when the universe seems to have finished reionization. This suggests that reionization is an extended process, starting as early as  $z \sim 15 - 20$ , and it has become clear that the majority of ionizing photons originate from stellar sources (e.g., Dijkstra et al. 2004; Fan et al. 2006; Willott et al. 2010; Zahn et al. 2012; Bouwens et al. 2012; Haardt & Madau 2012; Becker & Bolton 2013). X-ray radiation with its much longer mean free path than UV radiation has been considered a good candidate for the pre-ionization and pre-heating much earlier than  $z \sim 6$  (e.g., Oh 2001; Venkatesan et al. 2001; Ricotti & Ostriker 2004; Ricotti et al. 2005). In case the integrated electron abundance by UV sources is not sufficient to explain the observed high value of  $\tau_e$ , X-ray sources may generate additional electrons during epoch of reionization (EoR) to compensate for such deficiency. X-ray pre-heating might have significant impacts on the 21 cm signatures of reionization at high redshifts (e.g., Mesinger et al. 2013; Fialkov et al. 2014). Detecting these signals is a very hard task with the current radio facilities, but recent 21 cm observation of EoR by PAPER (Parsons et al. 2013) has suggested that the IGM at  $z = 7.7$  may have been pre-heated by X-rays. Two major candidates of X-ray sources are active galactic nuclei (AGNs) and X-ray binaries (XRBs) of metal-enriched stars. However, these sources appear in the universe late ( $z \lesssim 10$ ) and might be too weak to have an important impact on the reionization history. In addition to these two candidates, Pop III stars and their remnants are possible candidates for strong X-ray emission. Pop III in the approximate mass range  $40 - 140M_\odot$  and  $> 260M_\odot$  may directly collapse to form black holes (BHs; Heger et al. 2003). Any strong accretion onto these massive Pop III seeding BHs would lead to X-ray radiation at high redshifts (Kuhlen & Madau 2005; Alvarez et al. 2009; Tanaka et al. 2012). Supporting this additional avenue of radiation sources during reionization, recent cosmological simulations (Turk et al. 2009; Stacy et al. 2010; Stacy & Bromm 2013) have found that metal-free star-forming clouds might fragment to form binaries in a non-negligible fraction of Pop III star-forming events, which are promising X-ray sources at high redshifts.

The emerging X-rays from these binaries might be excellent sources of IGM pre-heating and pre-ionization for several reasons. They form at very high redshifts, so there is ample time for X-rays to heat and ionize the IGM, which is important because the ionization and

heating timescales can be a sizable fraction of the Hubble time. A top-heavy IMF favors BH formation on the order of tens of solar masses, whose luminosity are much higher than the late-type solar mass binaries, and their radiation is strong at  $\sim 1$  keV, which aids in escaping deep into the IGM, heating and partially ionizing the neutral gas in its path. X-ray radiation from Pop III binaries has been suggested to produce a pre-heated IGM (e.g., Mirabel et al. 2011; Haiman 2011; Mesinger et al. 2013) and, more relevant to reionization, may partially ionize the IGM in large volumes (e.g., Ostriker & Gnedin 1996; Pritchard & Furlanetto 2007).

X-ray pre-heating and pre-ionization on large scales might also be important for the later structure formation (Tanaka et al. 2012). For example, at high redshift, heating from the CMB may limit the radiative cooling, and thus increasing the Jeans mass, resulting in an IMF that also favors massive star formation for Pop II stars (Larson 2005; Smith et al. 2009). X-rays may also play the same role to heat the IGM and change the IMF of the Pop II stars. The impact of X-rays from Pop III binaries has been tested by some recent cosmological simulations. By considering X-ray feedback from Pop III binaries in a  $1 \text{ Mpc}^3$  volume simulation, Jeon et al. (2013) found that although no strong effects on star formation history from the X-ray feedback were found, the preheating of the IGM X-rays may lead to a suppression of small-scale structures and lower the recombination rate in the IGM, which could accelerate the reionization process.

X-rays from Pop III binaries are believed to be important for reionization, and cosmic structure formation, and have been studied by semi-analytic models (e.g. Power et al. 2009; Mirabel et al. 2011; Mesinger et al. 2013) and small-volume cosmological simulations (Jeon et al. 2013). In this paper, we focus on using our results of Pop III formation in high-redshift galaxies in a large survey volume of over 100 comoving  $\text{Mpc}^3$  to understand the production and propagation of X-rays from Pop III binaries, the corresponding X-ray background, and their impact on the thermal and ionization state of the IGM. This paper is organized as follows. We first describe our simulation and XRB model in Section 2. Then in Section 3, we present evolution and distribution of X-ray emissions from Pop III binaries. We study the X-ray propagation, heating, and ionizing in the nearby IGM using ray tracing in Section 4. In Section 5, we present our model of the X-ray background and our estimations of the background and their effects on the IGM. Finally, we conclude this study with a summary and a discussion of X-ray background from Pop III binaries in the early universe, their IGM heating and ionization, and possible observable effects in Section 6.

## 2. SIMULATION AND X-RAY BINARY MODEL

### 2.1. Radiation Hydrodynamics Simulation: “Rarepeak”

We further analyze the simulation in Xu et al. (2013) to study possible X-ray radiation from Pop III binaries in the high-density  $\sim 138$  comoving  $\text{Mpc}^3$  survey volume. The simulation is performed using the adaptive mesh refinement (AMR) cosmological hydrodynamics code Enzo (Bryan et al. 2014). The adaptive ray-tracing module *Enzo+Moray* (Wise & Abel 2011) is used for the radiation transfer of ionizing radiation, which is coupled to

the hydrodynamics and chemistry in Enzo.

The initial conditions for the simulation is generated using MUSIC (Hahn & Abel 2011) with second-order Lagrangian perturbations at  $z = 99$ . We use the cosmological parameters from the 7-year WMAP  $\Lambda\text{CDM}+\text{SZ}+\text{LENS}$  best fit (Komatsu et al. 2011):  $\Omega_M = 0.266$ ,  $\Omega_\Lambda = 0.734$ ,  $\Omega_b = 0.0449$ ,  $h = 0.71$ ,  $\sigma_8 = 0.81$ , and  $n = 0.963$ . We use a hydrogen mass fraction  $X = 0.76$ . We simulate a comoving volume of  $(40 \text{ Mpc})^3$  that has a  $512^3$  root grid resolution and three levels of static nested grids centered on a high-density region. We first run a  $512^3$  N-body-only simulation to  $z = 6$ . Then we select the Lagrangian volume (a single rectangular box) around two  $\sim 3 \times 10^{10} M_\odot$  halos at  $z = 6$  and re-initialize the simulation, having the Lagrangian volume at the center, with three more static nested grids to have an effective resolution of  $4096^3$  and an effective dark matter mass resolution of  $2.9 \times 10^4 M_\odot$  inside the highest nested grid, which just covers the Lagrangian volume, with a comoving volume of  $5.2 \times 7.0 \times 8.3 \text{ Mpc}^3$  ( $\sim 300 \text{ Mpc}^3$ ). During the course of the simulation, we allow a maximum refinement level  $l = 12$ , resulting in a maximal resolution of 19 comoving pc. The refinement criteria employed are the same as in Wise et al. (2012b). The refinements higher than the static nested grids are only allowed in a sub-volume, which adjusts its size during the simulation to contain only the highest-resolution dark matter particles, of the highest static nested grid. The highly refined region, covering the Lagrangian volume of the two massive halos at  $z = 6$ , has a comoving volume of  $3.8 \times 5.4 \times 6.6 \text{ Mpc}^3$  ( $\sim 138 \text{ Mpc}^3$ ) at  $z = 15$ , which represents a  $3.5\sigma$  density peak. We call this well-resolved volume, which is also our survey volume, the Rarepeak in this study and related papers (Chen et al. 2014; Ahn et al. 2014). At this time, the simulation has more than ten thousand Pop III stars and remnants distributed over three thousand halos, most of them are more massive than  $10^7 M_\odot$ . The simulation has 1.3 billion computational cells in the refined region and consumed more than 10 million CPU hours on the Kraken system at NICS and Blue Waters system at NCSA.

### 2.2. Star Formation and Feedback

Both Pop II and Pop III stars are allowed to form inside the survey volume, and we distinguish them by the total metallicity of the densest star-forming cell. Pop III stars are formed if  $[Z/H] < -4$ , and Pop II stars are formed otherwise. We use the same star formation models and most of the parameters as in Wise et al. (2012b), as well as feedback models. For the initial mass of Pop III stars, we randomly sample from an IMF with a functional form:

$$f(\log M)dM = M^{-1.3} \exp \left[ - \left( \frac{M_{\text{char}}}{M} \right)^{1.6} \right] dM \quad (1)$$

which behaves as a Salpeter IMF above the characteristic mass,  $M_{\text{char}}$ , but is exponentially cutoff below that mass (Chabrier 2003). Here, we use a characteristic mass of  $40 M_\odot$  for the Pop III IMF, which agrees with the latest results of Pop III formation simulations (e.g., Turk et al. 2009; Greif et al. 2012). For the details of the star formation and stellar feedback schemes used, refer to Sections 2.2 and 2.3 of Wise et al. (2012b).

The simulation performs ray tracing to calculate the propagation of UV H I ionizing radiation, but to study the X-ray radiation transport and associated photoheating and photoionization effects from Pop III binaries, we post-process the data sets with *Enzo+Moray* to calculate the X-ray radiation transport, which also includes the ionization of He I and He II. We consider secondary ionizations and heating by X-ray photons, using the fitting formula from Shull & van Steenberg (1985). Details of the implementation can be found in Wise & Abel (2011).

### 2.3. X-Ray Model of Pop III Binaries

We first need to use our Pop III distribution from simulation to estimate the X-ray radiation from Pop III binaries. Since the occurrence fraction, properties, and evolution of Pop III binaries are not yet well constrained (e.g., Stacy & Bromm 2013), we build a simple model, which takes advantage of solid information on Pop III population and distribution and ignores the details of Pop III binary formation and evolution, to estimate the X-ray luminosities from Pop III binaries in Rarepeak. We ignore the Pop III star initial mass, when we set the chance of a Pop III becoming binary and the evolution of the companion star. We assume that there is  $\alpha$  ( $0 \leq \alpha \leq 1$ ) chance that a Pop III star becomes an XRB. We also assume that one companion directly collapses into a BH with a mass of tens of  $M_\odot$  without a supernova (Fryer 1999), and the remaining mass exists in the companion star. In addition, the companion star is supposed to live as a normal star (e.g., no SN or BH) for a constant lifetime  $\tau$ , no matter what its mass is. For simplicity, we set the initial  $M_{\text{BH},0}$  to  $40 M_\odot$  if the Pop III star particle mass ( $M_\star$ ) is more massive than  $40 M_\odot$ , or  $10 M_\odot$  if  $10 M_\odot < M_\star < 40 M_\odot$ . We do not consider XRB formation in Pop III stars smaller than  $10 M_\odot$ . The initial BH mass should be a free parameter in the model. However, considering that it introduces too much complication into the accretion and X-ray spectrum modeling, we simply fix them here. The BH then accretes matter from the companion star at the Eddington limit during the lifetime of the companion star  $\tau$ , which we take to be a free parameter in our model, or until all the mass of the companion star accretes onto the BH. We will discuss the effects of different  $\tau$  on the X-ray luminosity in the next section. We do not consider the accretion from environment, so once the BH ceases accretion from the secondary star, its X-ray luminosity is zero. When electron scattering dominates opacity, the isotropic luminosity from accretion is limited to the Eddington luminosity,

$$L_{\text{Edd}} = 1.3 \times 10^{38} \left( \frac{M_{\text{BH}}}{M_\odot} \right) \text{ erg s}^{-1} \quad (2)$$

The radiation efficiency of accretion is  $\epsilon = L/\dot{M}c^2$ , so the mass accretion rate at the Eddington limit is  $\dot{M}_{\text{Edd}} = L_{\text{Edd}}/\epsilon c^2$ . Then, the mass evolution of the BH is

$$M_{\text{BH}} = M_{\text{BH},0} \exp \left( \frac{t}{t_{\text{Edd}}} \right) \quad (3)$$

where the Eddington time  $t_{\text{Edd}} = M_{\text{BH}}/\dot{M}_{\text{Edd}} = \epsilon c^2 M_\odot / 1.3 \times 10^{38} \text{ erg s}^{-1} \sim 440\epsilon \text{ Myr}$  before the companion star runs out of matter.

Since we only update the X-ray luminosity of snapshots between large time steps ( $\delta z \sim 0.5$ ), which is  $\sim 6$  and  $12 \text{ Myr}$  at  $z = 20$  and  $15$ , respectively, we use the time averaged luminosity as the luminosity of each Pop III binary. The total BH accreted mass is

$$M_{\text{acc}} = \begin{cases} M_{\text{BH},\text{max}} - M_{\text{BH},0} & \text{for } M_\star > M_{\text{BH},\text{max}} \\ M_\star - M_{\text{BH},0} & \text{for } M_\star \leq M_{\text{BH},\text{max}} \end{cases} \quad (4)$$

where  $M_{\text{BH},\text{max}} = M_{\text{BH},0} \exp \left( \frac{\tau}{t_{\text{Edd}}} \right)$  is the maximum mass of a BH after accreting at the Eddington limit for the lifetime  $\tau$ .

The total radiation energy from the accretion process is  $\epsilon M_{\text{acc}} c^2$ , so the average luminosity of each binary is simply  $\epsilon M_{\text{acc}} c^2 / t_{\text{acc}}$ , where the accretion time  $t_{\text{acc}}$  is  $\tau$  for  $M_\star > M_{\text{BH},\text{max}}$ , or  $\ln(M_\star/M_{\text{BH},0}) t_{\text{Edd}}$  for  $M_\star \leq M_{\text{BH},\text{max}}$ . There is no delay between BH and Pop III formation considered; each Pop III binary luminous X-ray radiation is at this constant rate since the Pop III star forms in the simulation for its accretion time  $t_{\text{acc}}$ . Using this model, the X-ray energy output is simply determined by the three free parameters, lifetime  $\tau$ , binary probability  $\alpha$ , and radiation efficiency  $\epsilon$ .

The propagation of X-ray radiation and the effects on the IGM are dependent on the photon energy because the H I cross-section approximately decreases rapidly as  $\sim \nu^{-3}$ . Although, in post-processing, we consider a monochromatic spectrum and not a spectral energy distribution (SED), we can estimate the effects of different XRB SEDs by exploring different photon energies. We adapt a multi-color disk (MCD) blackbody (Mitsuda et al. 1984) plus a high-energy power-law model to model the radiation spectrum from Pop III binaries with BHs with masses of tens of  $M_\odot$ . This model was also adopted for mini-quasars in a cosmological context in Kuhlen & Madau (2005), who considered the photoheating and photoionization effects from a  $150 M_\odot$  BH that has a softer SED than the binaries presented in this work. Their model included a MCD component with luminosities equally divided between a multi-color disk and a power law component with a power index  $\alpha$  both with the same low-energy cutoff. In a MCD model, each annulus of a thin accretion disk radiates as a blackbody with a radius-dependent temperature,  $T(r) \propto r^{-3/4}$ , and the temperature of the innermost portion of the disk decreases slowly with BH mass (Makishima et al. 2000) as  $T_{\text{in}} \sim 1.2(M_{\text{BH}}/10M_\odot)^{-1/4} \text{ keV}$ . The inner disk temperature is about  $1.2 \text{ keV}$  and  $0.8 \text{ keV}$  for a  $10 M_\odot$  and  $40 M_\odot$  BH, respectively. We use a similar SED functional form as Alvarez et al. (2009), assuming  $L_\nu \propto \nu$  for  $h\nu < 400 \text{ eV}$ ,  $L_\nu \propto \nu^{-1}$  for  $400 \text{ eV} < h\nu < 10 \text{ keV}$ , and  $L_\nu = 0$  for  $h\nu > 10 \text{ keV}$ , which has a mean photon energy of  $\sim 770 \text{ eV}$ . To study the effects of different photon energies, we consider several different monochromatic photon energies ( $E_{\text{ph}}$ ) between  $300 \text{ eV}$  to  $3 \text{ keV}$ , covering most of the emissions from this model.

### 3. X-RAY LUMINOSITY FROM RAREPEAK

We present the evolution of the X-ray luminosity from Pop III sources and its distribution among halos in our Rarepeak survey volume in this section. We first need to choose the free parameters for our X-ray model. We

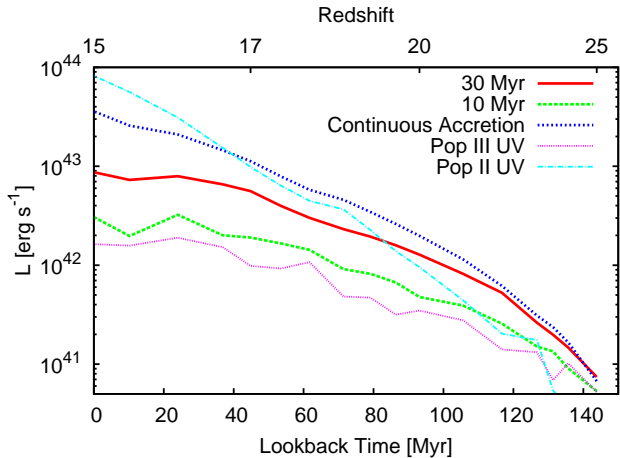


**Figure 1.** Evolution of total X-ray luminosities from Pop III binaries in the Rarepeak region with two assumed lifetimes of the binary companion stars. In the case of all Pop III BH continuously accreting at the Eddington limit (the blue dotted curve), their total luminosity is about four times that of the 30 Myr case at  $z = 15$ . The luminosities of hydrogen ionizing photons from Pop II and Pop III stars in the simulation are shown for reference. The UV radiation from Pop II stars dominates the radiation feedback from  $z \sim 19$ .

try two companion star lifetimes  $\tau = 10, 30$  Myr. We set the probability for a Pop III star becoming an XRB to  $\alpha = 0.5$ . This assumes that there is a high binary fraction, comparing to 0.36 in Stacy & Bromm (2013), and almost all Pop III binaries are XRBs. The radiation efficiency depends on the BH properties. It is 0.057 for a Schwarzschild BH, and increases to  $\sim 0.4$  for a prograde disk around a maximally rotating BH (Thorne 1974), and could be even higher for a magnetized disk (Gammie 1999). Here, we simply set it to  $\epsilon = 0.2$ . We choose this number higher than other studies (e.g., Ricotti & Ostriker 2004; Alvarez et al. 2009), making the growth of BH slower and the total X-ray radiation weaker ( $\sim 20\%$  comparing to  $\alpha = 0.1$ ). Since both the binary lifetime  $\tau$  and XRB probability only impact the X-ray luminosity linearly, our results are easily adjusted with different parameters when better constraints are available.

Figure 1 shows the evolution of the total X-ray luminosity for two different binary lifetimes  $\tau = 10, 30$  Myr. We also plot the UV hydrogen ionizing photon luminosities from both Pop III and Pop II stars to compare with X-rays. The X-ray luminosity follows the Pop III formation rate (see Figure 1 in Xu et al. 2013) and thus the UV luminosity of Pop III stars. The total X-ray output steadily increases until the simulation ends at  $z = 15$ , where  $L_X = 8 \times 10^{42} \text{ erg s}^{-1}$ , which is consistent with that in Mirabel et al. (2011). The X-ray dependence on the binary lifetime is simple and linear, so that the luminosity from the 30 Myr case is always 2–3 times higher than the  $\tau = 10$  Myr scenario. X-ray radiation from Pop III binaries dominates the total luminosity budget until the most massive halos begin to form Pop II stars efficiently.

X-ray production from Pop III stars is debatable because of the uncertainties in models of metal-free binary evolution. To calculate the upper limit of the X-ray luminosity in our simulation, we consider the unlikely case where BHs in Pop III binaries continuously accrete at

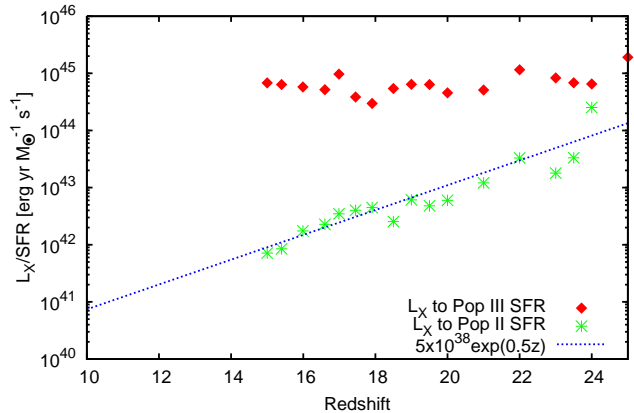


**Figure 2.** Ratios of X-ray luminosity to the Pop III and Pop II star formation rates.

the Eddington limit after formation. This is shown as a dotted blue line in Figure 1. At  $z > 20$ , this optimistic scenario is comparable to the  $\tau = 30$  Myr case, because at that redshift, most Pop III binaries are still active. At  $z = 15$ , it is about four times higher than the  $\tau = 30$  Myr model, suggesting that we are not underestimating the X-ray output significantly even in the worst scenario.

Next, we compute the relationship between the X-ray luminosity and Pop II and III star formation rates (SFRs), which are shown in Figure 2, for the  $\tau = 30$  Myr case. X-ray output closely follows the Pop III star formation as  $L_X \sim 5 \times 10^{44} \text{ erg s}^{-1} (\text{SFR}_{\text{III}} / M_{\odot} \text{ yr}^{-1})$ . This is expected in our model because X-ray luminosity is proportional to the Pop III SFR within the past 30 Myr. The X-ray luminosity can also be correlated to the Pop II SFR over time,  $L_X \sim 5 \times 10^{38} \exp(0.5z) (\text{SFR}_{\text{II}} / M_{\odot} \text{ yr}^{-1}) \text{ erg s}^{-1}$  in the range  $z = 15 - 25$ , which decreases in time simply due to the increasing Pop II SFR. By extrapolating this relation to lower redshifts, we can determine that  $L_X$  from Pop III binaries become comparable to the scaling relation found in local starburst galaxies (e.g., Oh 2001), which happens at  $z \sim 9$  when  $L_X \sim 5 \times 10^{40} (\text{SFR}_{\text{II}} / M_{\odot} \text{ yr}^{-1}) \text{ erg s}^{-1}$ .

A correction factor  $f_X$  for X-ray efficiency is commonly used in the literature to relate the SFR and the X-ray luminosity. Using the same definition as Furlanetto (2006),

$$L_X = 3.4 \times 10^{40} f_X \left( \frac{\text{SFR}}{M_{\odot} \text{ yr}^{-1}} \right) \text{ erg s}^{-1}, \quad (5)$$

we find that  $f_X \simeq 1.5 \times 10^4$  and  $f_X \simeq 0.015 \exp(0.5z)$  for Pop III and Pop II stars, respectively. While  $f_X$  for Pop II stars is lower than that for Pop III stars (due to Pop II-dominated SFRs), it is still much larger than  $f_X(\text{Pop II})$  for normal galaxies. Low-redshift starbursts were estimated to have  $f_X < 1.7$  (e.g., Oh 2001; Fragos et al. 2013), while here,  $f_X(\text{Pop II}) = [27-330]$  at  $z = [15-20]$ .

The distributions of X-ray luminosity from Pop III binaries among halos at  $z = 15$  and 17.9 for the  $\tau = 10$  and 30 Myr models are shown as functions of halo mass in Figure 3. Unsurprisingly, the distributions reflect the same halo mass dependence as the Pop III stars and remnants (see Figure 3 in Xu et al. (2013)). The peak of X-ray luminosity is at  $\sim 2 \times 10^7 M_{\odot}$  and most of the

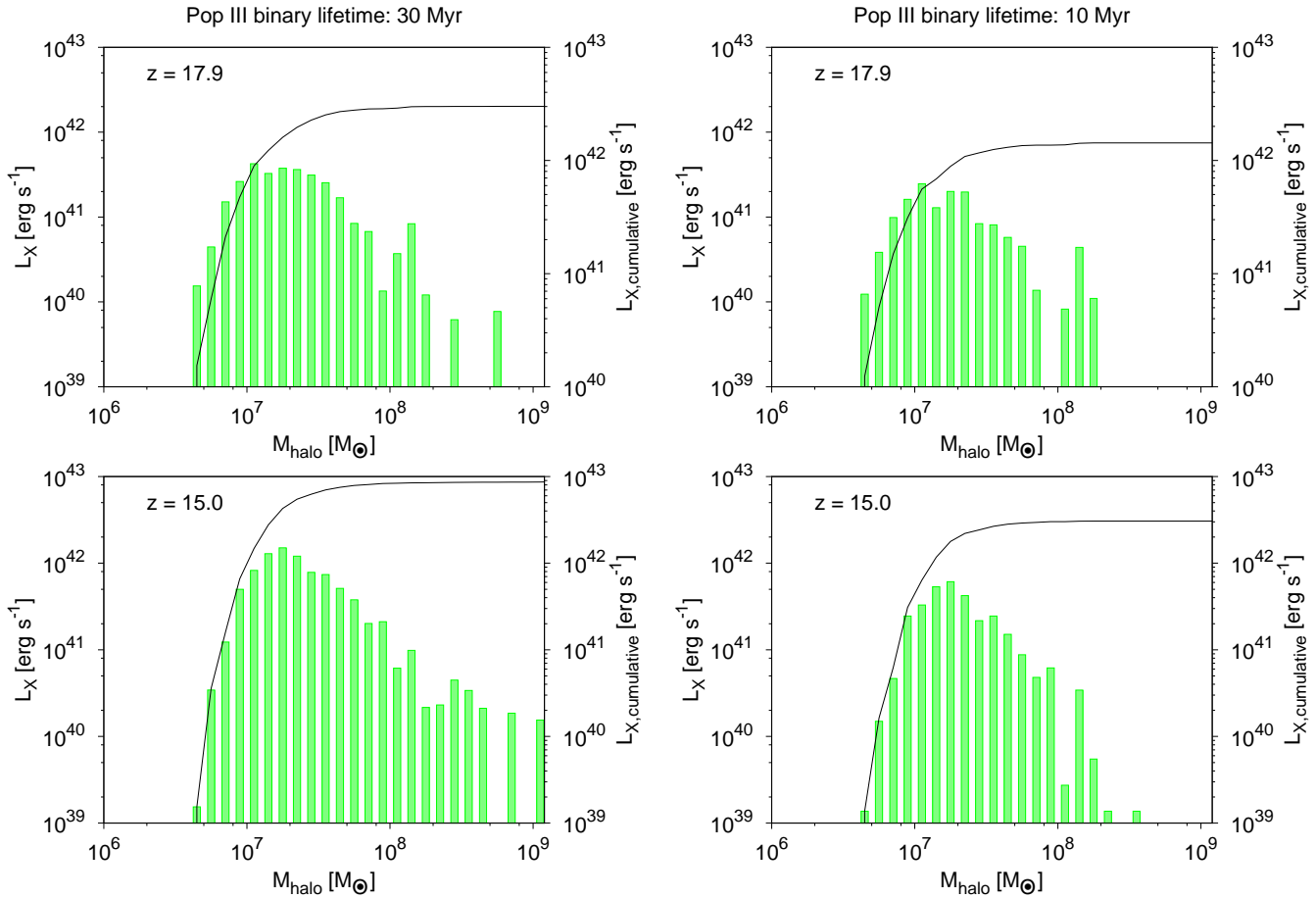


**Figure 3.** Distributions of X-ray luminosity from Pop III binaries over halo mass in the Rarepeak region of 10 Myr (right) and 30 Myr (left) cases at  $z=17.9$  (top) and  $z=15$  (bottom). The black line is the cumulative X-ray luminosity.

X-rays are from small halos that have a small neutral column density, allowing for a large X-ray escape fraction.

We now turn our attention to the details of the resulting X-ray radiation field, using *Enzo+Moray*, adaptive ray tracing (Wise & Abel 2011), to calculate the X-ray propagation into the IGM.

#### 4. X-RAY HEATING, IONIZATION, AND ESCAPE FRACTIONS

Here we present results from calculating the X-ray radiation field by ray tracing its propagation to better understand how it photoheats and photoionizes the host halos, the Rarepeak region, and the IGM of the entire simulated volume. The long mean free paths of X-rays make it currently computationally unfeasible to trace rays from all the sources self-consistently within the original time-dependent cosmological simulation. To work around this limitation, we introduce some approximations and post-process our simulation to calculate the X-ray radiation field and to study its effects on the thermal and ionization state of the gas.

Because UV radiative transfer was included in the simulation, we only consider the transport of X-rays in post-processing. Starting with each output of the full simulation, we consider the matter field to be static and equal to the output at time  $t^n$  and allow the chemistry and energy solvers to evolve the ionization and thermal states of the

gas, using the calculated X-ray radiation field, until the time  $t^{n+1}$  of the next simulation output. Furthermore, we approximate multiple X-ray sources within a given halo as a single point source at the halo center with a luminosity representing the sum of all active X-ray Pop III binaries in each halo. For the X-ray luminosity of a halo in each post-processing timestep, we calculate the average luminosity of the halo as  $\langle L_{X,\text{halo}} \rangle \equiv E_X / (t_1 - t_0)$ , where  $E_X$  is the total X-ray energy by all sources in the halo that is emitted between the earliest formation time  $t_0$  and latest cessation time  $t_1$  of X-ray-emitting Pop III binaries.<sup>5</sup> We should mention that this approach results in a slightly different (a few percent) total luminosity as in the previous section, but this difference does not manifest into appreciable changes in the thermal and ionization states of the gas, especially when considering the uncertainty in X-ray luminosities of Pop III binaries. Finally, we consider absorption by neutral and singly ionized helium, which is important at these high energies, which was neglected in the stellar UV radiation transport in our original calculation.

We run the ray tracing post-processing using a single energy group of 300 eV, 500 eV, 1 keV or 3 keV, cov-

<sup>5</sup> The earliest formation and latest cessation times are restricted by the time elapsed in the post-processing timestep, i.e.,  $t_0 = \max(t_0, t^n)$  and  $t_1 = \min(t_1, t^{n+1})$ .

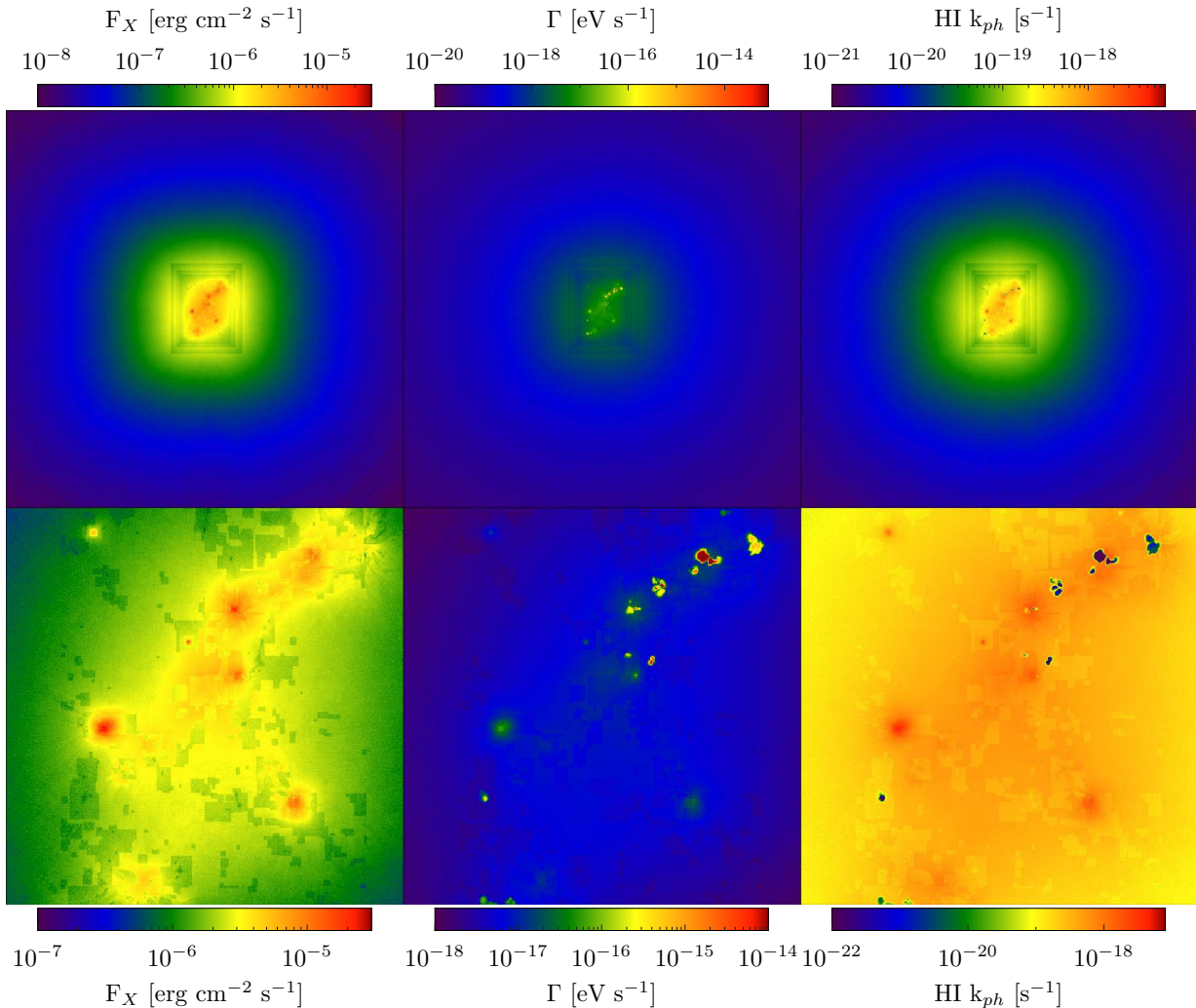


**Figure 4.** Slices of X-ray flux  $F_X$  (left), X-ray photoheating rate  $\Gamma$  (middle) and X-ray H I photoionization rate  $k_{ph}$  (right) of the ray-tracing run with 1 keV photon energy at  $z = 15$ . The top panels are images through the entire box (40 comoving Mpc on a side), and the bottom panels show the zoomed-in central squares of 5 comoving Mpc on a side. Out of the high-density region, Rarepeak works just like an X-ray point source. The zoomed-in images show some H II regions with high photoheating rates and low H I ionization rates. Because the high-resolution cells are not sampled by enough rays after ray splitting turned off at a large radius, there are some grid artifacts in thin layers at the refined and nested region boundaries, as well as in the zoomed-in images.

ering most of the spectrum of XRBs with tens to one hundred  $M_{\odot}$  BHs. In Figure 4, we show the slices of X-ray flux, photoheating rate  $\Gamma$  and H I photoionization rate  $k_{ph}$  through the center of the simulated volume to illustrate the distribution and effects of the X-rays for the 1 keV case at  $z = 15$ . There are grid artifacts at the refined and nested grid boundaries. This is due to the smaller cells which are not sufficiently sampled by enough rays (Wise & Abel 2011) as we turn off the ray splitting once a ray has traveled more than 320 comoving kpc to save memory. These artifacts do not affect our results since they only occur in thin layers. As expected, X-rays can easily travel out of the hosting halos and Rarepeak region into the normal IGM. Although X-ray sources inside Rarepeak show complicated structures, the X-ray radiation field outside of the Rarepeak are quite spherically symmetric. The ionization and heating timescales are sufficiently low so that the IGM properties do not change considerably, and the X-rays travel through the IGM passively, eventually reaching a steady state well

before the next post-processing timestep.

The volume-averaged radial profiles of X-ray intensity, photoheating rate  $\Gamma$  and H I photoionization rate  $k_{ph}$  for different photon energies are shown in Figures 5, 6, 7, respectively. No obvious evolution is observed for these quantities from the two shown redshifts,  $z = 17.9$  and 15. There are very different features between the results for hundreds eV (“sub-keV”) and keV photons.

#### 4.1. X-Ray Intensity

X-ray intensities are almost flat inside the Rarepeak and decrease externally because we do not consider star formation outside of the Rarepeak.

1. Sub-keV Photons. The 300 and 500 eV X-ray intensities are much weaker than keV ones because the absorption is stronger at lower photon energies. Their intensities drop fast outside of the source region. Only small amounts of photons escape to the IGM. More specifically, at  $z = 15$ , there are about 15.8% and 50.5% of the total X-ray energy escaping the Rarepeak region at 200 kpc ra-

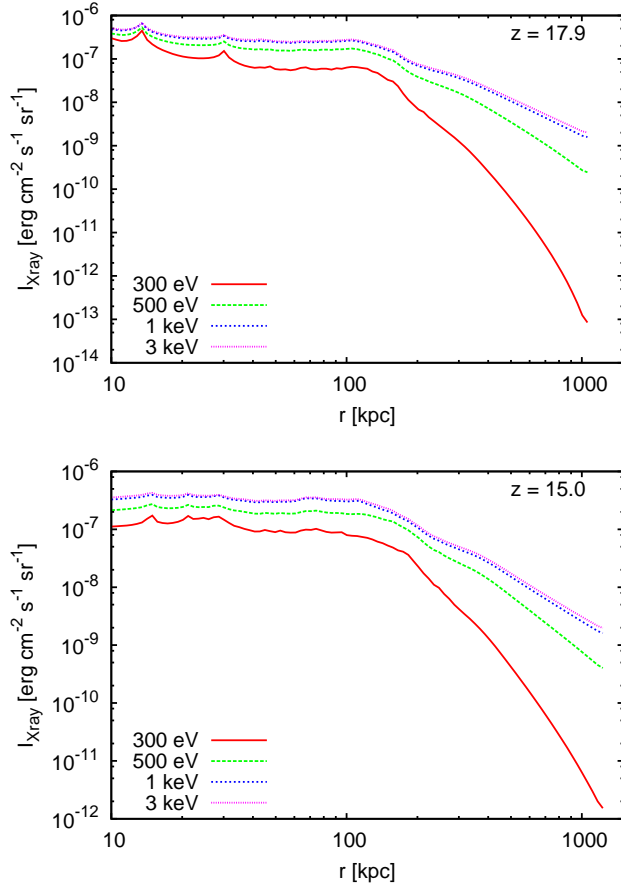


**Figure 5.** Volume-averaged distribution of X-ray intensities as a function of the distance to the center of the simulated volume at  $z=17.9$  (top) and  $z=15$  (bottom). The X-rays are ray traced by post-processing. Different lines represent the results from different photon energies, while the luminosity of the sources are the same.

dius (3.2 comoving Mpc) for 300 eV and 500 eV photons, respectively. At 1 Mpc (16 comoving Mpc) radius, the escape fractions are only 0.11% and 13.1%, respectively.

2. KeV photons. The attenuation of the keV photons through the IGM is weak, resulting in their intensities dropping just slightly faster than  $1/r^2$  geometric dilution. This leads to a significant amount of radiation at keV energy scales escaping into the IGM and possibly contributing to the X-ray background. At  $z = 15$ , there are about 73.9% and 81.0%, of the total X-ray energy escaping the Rarepeak region at 200 kpc radius (3.2 comoving Mpc) for 1 keV and 3 keV cases, respectively. At 1 Mpc (16 comoving Mpc) radius, the escape fractions are 44.3% and 53.2%, respectively.

#### 4.2. X-Ray Photoheating

The radial distribution of X-ray photoheating rates is more complicated than that of X-ray intensities. There is a large variance inside the Rarepeak because the heating rates are highest in star-forming halos, which have high electron fractions and thus have most of the photon energy deposited to thermal energy.

1. 300 eV Photons. Because the attenuation of low-energy photons through H I, He I, and He II are much higher (recall that their cross-sections scale as  $\sim 1/E_{\text{ph}}^3$ ),

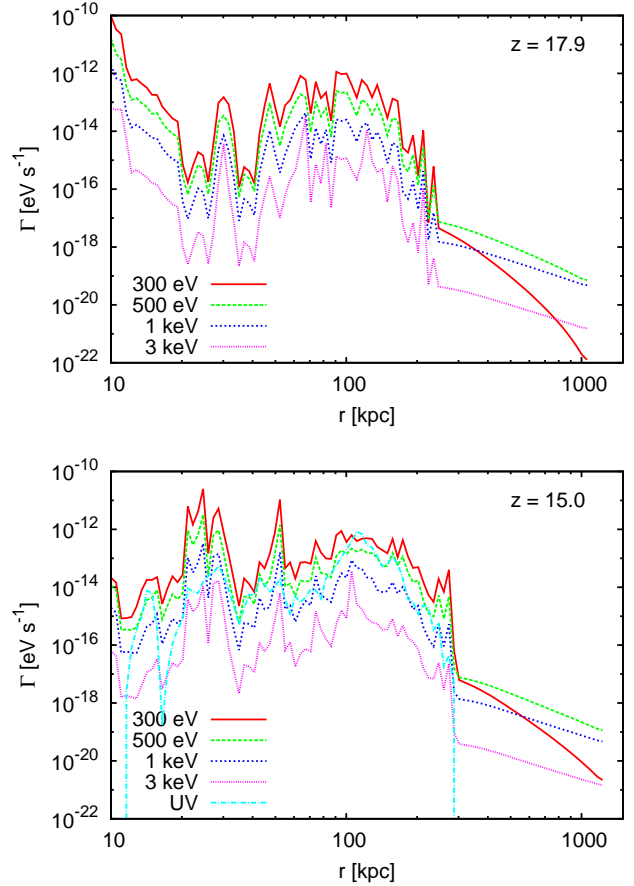


**Figure 6.** Same as Figure 5, but for the X-ray photoheating rate  $\Gamma$ . We also plot the profile of the UV photoheating rate at  $z=15$  from the original simulation.

high heating rates are created by these low-energy photons, which extend to the boundary of the Rarepeak region. The X-ray photoheating can significantly change the thermal state of the gas inside the Rarepeak in just millions of years.

2. 500 and 1 keV Photons. Photons at this energy range heat the Rarepeak region more weakly, but can efficiently heat the IGM when compared to lower-energy photons. However, their overall rates are not high, and they need a long time to significantly increase the IGM temperature.

3. 3 keV Photons. Though the 3 keV photon intensity is strong, weak interactions between high-energy photons and gas result in very low heating rates.

We also plot the photoheating rate profile at  $z = 15$  from the UV ionizing photons that were originally included in the simulation to illustrate the significance of X-ray heating. The spherically averaged UV heating rate is comparable to the X-ray photoheating inside the Rarepeak and drops to almost zero out of the star-forming region because the UV photons are all absorbed within a few kpc of their origins. Because the UV radiation can only heat the gas within these small-scale H II regions, the thermal morphology from UV radiation is porous, whereas the X-ray radiation creates a smoothly varying component of the heated IGM.

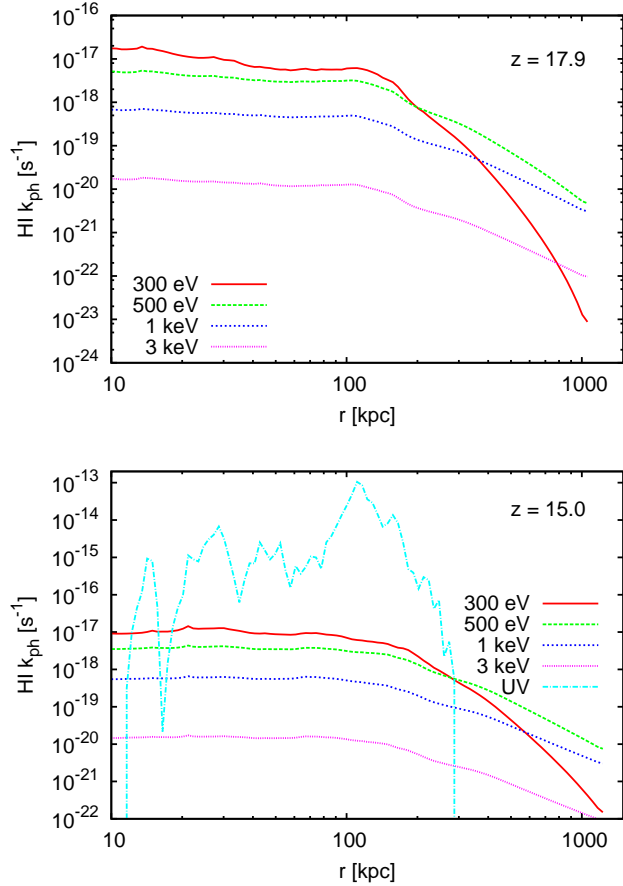


**Figure 7.** Same as Figure 5, but for the X-ray H I photoionization rate  $k_{ph}$ . We also plot the profile of the UV photoionization rate at  $z=15$  from the original simulation.

#### 4.3. X-Ray Photoionization

The distribution of H I photoionization rates  $k_{ph}$  for different photon energies is similar to the photoheating rate  $\Gamma$ , but their profiles are much smoother inside the Rarepeak.

1. 300 eV Photons. The 300 eV photons have relatively high photoionizing rates inside Rarepeak and extend to the edge of the Rarepeak. But at rates of  $\sim 10^{-17} \text{ s}^{-1}$ , they are insignificant compared to the UV photoionization for the star-forming region of Rarepeak.

2. 500 and 1 keV Photons. Similar to our photoheating results, radiations in the 0.5–1 keV band are more efficient at photoionizing the IGM, where the Rarepeak acts as a single source at large distances, still at very low rates  $< 10^{-18} \text{ s}^{-1}$ .

3. 3 keV Photons. Their photoionization rates are much lower compared to lower photon energy cases in both Rarepeak and the IGM.

We also plot the profile of the photoionization rate at  $z = 15$  from the UV radiation. Contrary to the behavior in the heating rates, the photoionization by UV is much more efficient than the ionization by X-rays inside the Rarepeak, as a higher fraction of UV photon energies is used to ionize the IGM than to heat them. Outside of the Rarepeak region, the UV radiation is fully attenuated, and the photoionization rates drop to zero accordingly.

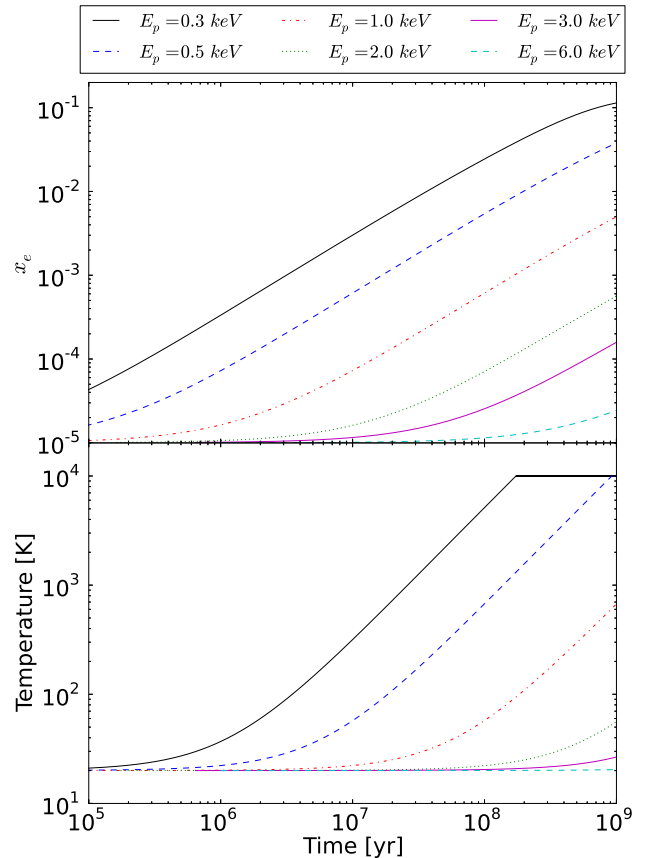


**Figure 8.** Evolution of the electron fraction (top) and temperature (bottom) from a one-zone calculation for different photon energies with the same X-ray flux  $10^{-6} \text{ erg cm}^{-2} \text{ s}^{-1}$ .

## 5. EFFECTS OF X-RAYS ON THE IGM

Ray tracing of X-rays is very computationally expensive because it is in the optically thin limit. Thus, it is not possible to perform the ray tracing self-consistently with all other physics and chemistry for the duration of the simulation. However, in the previous section, we showed that the X-ray ionization rates are low enough so that it does not dynamically affect the electron fraction of the IGM and then the opacity of X-rays and any ensuing star formation. In this limit, it is safe to assume that the X-ray intensity will remain constant in between outputs of the original simulation. We thus freeze the X-ray radiation field and use a simple model to study the X-ray photoheating and photoionization of the IGM.

### 5.1. One Zone Model of X-Ray Heating and Ionization

We first use a one-zone model to study the effects of X-rays of different photon energies and fluxes on the IGM. This model includes X-ray heating and ionization with secondary ionizations, collisional ionizations, recombinations (case B), and primordial atomic cooling. The changes of electron fraction ( $x_e$ ) and thermal energy ( $E_{th}$ ) are expressed as

$$\frac{dx_e}{dt} = (1 - x_e)(k_{ph} + n_e k_1) - x_e n_e \alpha_B \quad (6)$$

$$\frac{dE_{th}}{dt} = \Gamma_{ph} - \Lambda \quad (7)$$

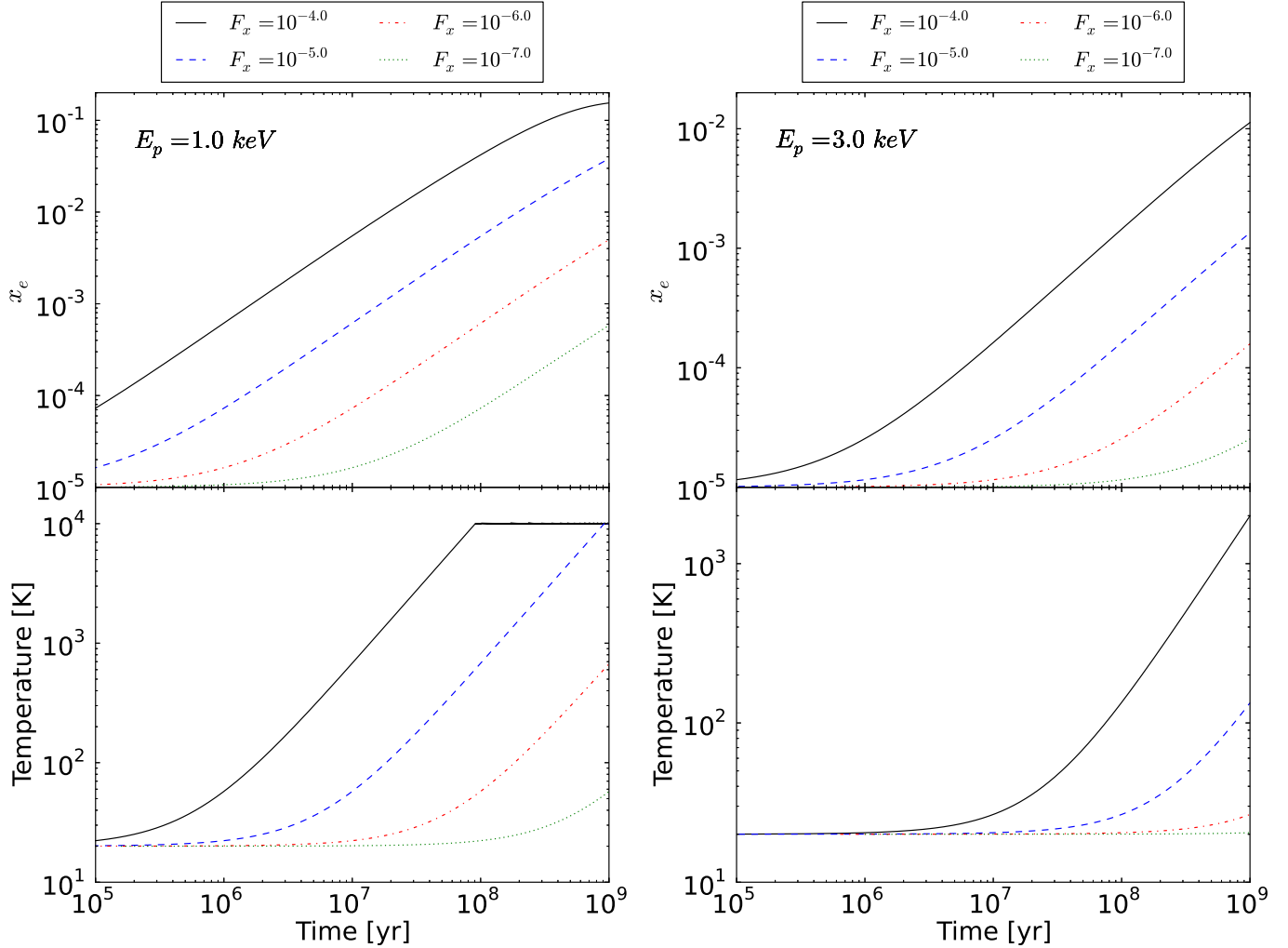


**Figure 9.** Evolution of the electron fraction (top) and temperature (bottom) from one-zone calculations of 1 keV and 3 keV photon energies with a variety of radiation fluxes.

Here, the photoionization and photoheating rates  $k_{ph}$  and  $\Gamma_{ph}$  with the X-ray secondary ionizations use the results from Shull & van Steenberg (1985), the same as in our ray tracing calculation (Wise & Abel 2011).  $k_1$  is the collisional ionization coefficient in Abel et al. (1997), using the fit in Janev et al. (1987). The case B recombination coefficient,  $\alpha_B$  is  $2.59 \times 10^{-13} (T/10^4 \text{ K})^{-0.7} \text{ cm}^{-3} \text{ s}^{-1}$  (Osterbrock 1989). The primordial atomic cooling rate  $\Lambda$  is computed using the table in Sutherland & Dopita (1993) when the gas temperature is over  $10^4 \text{ K}$ .

The model considers a constant X-ray flux impacting an initial cold ( $T = 20 \text{ K}$ ) and neutral ( $x_e = 10^{-5}$ ) gas parcel with mean cosmic density. The calculation starts at  $z = 15$  and evolves for 1 Gyr. The photon energy used in the calculation is not redshifted and is kept as a constant. Also, the decrease of temperature due to the expansion of the universe is not considered.

We first study the effects of different photon energies with an X-ray flux of  $10^{-6} \text{ erg cm}^{-2} \text{ s}^{-1}$ , which is close to the X-ray fluxes generated by Rarepeak in our ray-tracing simulations. We plot the evolution for the electron fraction and temperature in Figure 8 for this X-ray

flux of different photon energies in a range from 300 eV to 6 keV.

1. Sub-keV Photons. X-rays below 1 keV can significantly heat and ionize the IGM. The 300 eV case heats the gas to  $10^4 \text{ K}$  in  $\sim 100 \text{ Myr}$ , at which point atomic hydrogen cooling becomes efficient, resulting in an ionization boost of 10 percent, which is enough to contribute a non-negligible amount to the optical depth from Thomson scattering.

2. KeV Photons. The keV photons can only moderately heat the gas and weakly ionize the IGM. For 1 keV photons, even for 1 billion years, the gas temperature only reaches slight over 600 K and the electron fraction is just  $5 \times 10^{-3}$ , not high enough to impact the optical depth of the CMB from Thomson scattering. But this electron fraction is high enough to stimulate the  $H_2$  formation, and then, in turn, the Pop III star formation (Ricotti et al. 2001; Yoshida et al. 2004). For even higher photon energies, the heating and ionizing effects are negligible at this level of X-ray flux.

For keV radiation, stronger fluxes are needed to heat and ionize the IGM to a meaningful level. The evolution of the electron fraction and temperature is plotted in

Figure 9 for 1 keV and 3 keV photon energies with various X-ray fluxes. X-ray radiation of 1 keV photons with a flux of  $10^{-5}$  erg cm $^{-2}$  s $^{-1}$  can barely heat the gas to  $10^4$  K and ionize it to about 4%. This shows that for increasing the X-ray flux, the heating is more significant than the associated ionization. For 3 keV photons, even this elevated X-ray flux is not sufficient to heat and ionize the gas within 1 Gyr.

### 5.2. X-Ray Background Modeling

In a mean patch of the IGM, a small opacity for X-ray photons of  $E \gtrsim 1$  keV renders the mean free path truly cosmological ( $\sim$  a hundred comoving Mpc for 1 keV photons and several comoving Gpc for 3 keV photons). Therefore, we need to consider the X-ray background caused by sources outside the simulation box, in addition to the local transfer of X-ray photons. This is supported by our results in Section 4, showing that large amounts of keV X-rays easily escape out of their host halos, the Rarepeak region, and even the entire simulation box, which then contribute to the X-ray background. In this subsection, we describe our method that calculates the X-ray background from Pop III binaries.<sup>6</sup>

Our simulation only allow stars formed inside our refined Rarepeak region, which is only 0.22% of the entire survey volume, containing 0.37% of the total baryon mass. To compensate for these unresolved sources outside the Rarepeak region, we simply use the density distribution to populate X-ray sources out of the star-forming region in our simulation. We do not intend to establish a fully self-consistent correlation between X-ray luminosity from Pop III binaries and the underlying baryon density in such a coarse resolution, but our aim is to populate this region with X-ray sources in the most likely places. We first project the X-ray luminosity and baryon density to the root grid of  $512^3$ . For the cells with X-ray sources, we calculate the mean X-ray luminosity  $\bar{L}_{X,0}$  and baryon density  $\bar{\rho}_0$ . Then, for each cell in the region external to the Rarepeak with a baryon density higher than the mean density  $\bar{\rho}_0$ , we assume there is an X-ray source with luminosity  $\bar{L}_{X,0}$ . We find that sources populated in this manner produce X-ray luminosities that are several times higher than in the Rarepeak region alone. The total X-ray luminosities of the entire simulated volume are 6.7, 3.1, and 8.5 times those of Rarepeak region at  $z = 24, 17.9,$  and  $15,$  respectively.

In principle, the background itself can have spatial fluctuation due to the inhomogeneous distribution of radiation sources outside the simulation box. Nevertheless, simulating the structure formation on such a large scale, while resolving star-forming regions with the relevant local astrophysical processes in detail is almost impossible in practice at this time. Because inhomogeneity in the source distribution at large lookback times will be observed to be almost uniform inside the box, we simply treat the background sources to be uniformly distributed.

<sup>6</sup> We show in Section 4 that when the “normal” X-ray luminosity, which is calibrated from low-redshift galaxies (e.g. Fragas et al. 2013), is assigned to metal-enriched stars, its contribution to the X-ray background is negligible compared to that from Pop III binaries. Therefore, we simply ignore the X-rays from metal-enriched binaries in our simulation.

We also assume that the entire simulation box is a good representation of the average universe and takes its luminosity as the mean, globally averaged luminosity.

The (proper) X-ray background intensity  $J_\nu$  (erg s $^{-1}$  cm $^{-2}$  Hz $^{-1}$  sr $^{-1}$ ) at an observed frequency  $\nu$  and redshift  $z_{\text{obs}}$  will then be given by the following:

$$J_\nu(z_{\text{obs}}) = (1 + z_{\text{obs}})^3 \int_0^\infty \frac{dr_{\text{os}}}{1 + z_s} \bar{j}_{\nu_s}(z_s) \exp[-\tau_{\nu_{\text{obs}}}], \quad (8)$$

where  $\bar{j}_{\nu_s}$  (erg s $^{-1}$  cm $^{-3}$  Hz $^{-1}$  sr $^{-1}$ ) is the comoving emission coefficient given by

$$\bar{j}_{\nu_s} = \frac{1}{4\pi} \frac{L_{\nu_s, \text{Box}}(z_s)}{V_{\text{Box}}}, \quad (9)$$

where  $L_{\nu_s}$  (erg s $^{-1}$  Hz $^{-1}$ ) is the proper, total luminosity inside the simulation box at source frequency  $\nu_s$  and redshift  $z_s$ , and  $V_{\text{Box}}$  is the comoving volume of the simulation box. The optical depth originates from the absorption of photons by HI and HeI:

$$\begin{aligned} \tau_{\nu_{\text{obs}}} &= \tau_{\nu_{\text{obs}}, \text{HI}} + \tau_{\nu_{\text{obs}}, \text{HeI}} \\ &= \int_{t(z_s)}^{t(z_{\text{obs}})} c dt \\ &\quad \times \{ n_{\text{HI}}(z_s) \sigma_{\text{HI}}(\nu_s, z_s) + n_{\text{HeI}}(z_s) \sigma_{\text{HeI}}(\nu_s, z_s) \} \\ &= \int_{z_s}^{z_{\text{obs}}} \frac{c dz_s (1 + z_s)^{-5/2}}{H_0 \sqrt{\Omega_m}} \\ &\quad \times \{ n_{\text{HI}}(z_s) \sigma_{\text{HI}}(\nu_s, z_s) + n_{\text{HeI}}(z_s) \sigma_{\text{HeI}}(\nu_s, z_s) \}, \end{aligned} \quad (10)$$

where we neglect absorption by HeII, because the ionization fraction of the IGM at  $z \geq 15$  remains very low.  $r_{\text{os}}$  is the comoving line-of-sight distance that a photon has traveled given by

$$r_{\text{os}} = \frac{2c}{H_0 \sqrt{\Omega_m}} \left\{ (1 + z_{\text{obs}})^{-1/2} - (1 + z_s)^{-1/2} \right\}, \quad (11)$$

and the redshifted frequency  $\nu/\nu_s = (1 + z_{\text{obs}})/(1 + z_s)$ . Over the frequency range of our interest,  $100 \text{ eV} \lesssim h\nu \lesssim 3 \text{ keV}$ , absorption cross-sections are well approximated by power laws:

$$\sigma_{\text{HI}}(\nu_s) = 6.5 \times 10^{-14} \left( \frac{h\nu_s}{\text{eV}} \right)^{-3.25} \quad (12)$$

and

$$\sigma_{\text{HeI}}(\nu_s) = 1.55 \times 10^{-12} \left( \frac{h\nu_s}{\text{eV}} \right)^{-3.22}. \quad (13)$$

With these cross-sections, Equation (10) becomes

$$\begin{aligned} \tau_{\nu_{\text{obs}}} &= \left( \frac{\Omega_b}{0.044} \right) \left( \frac{h}{0.7} \right) \left( \frac{\Omega_0}{0.27} \right)^{-0.5} \left( \frac{1 + z_s}{1 + 25} \right)^{1.5} \\ &\quad \times \left\{ 4.10863 \left( \frac{X}{0.75} \right) \left( \frac{h\nu_0}{\text{keV}} \right)^{-3.25} \left[ \left( \frac{1 + z_s}{1 + z_{\text{obs}}} \right)^{1.75} - 1 \right] \right. \\ &\quad \left. + 10.13573 \left( \frac{Y}{0.25} \right) \left( \frac{h\nu_0}{\text{keV}} \right)^{-3.22} \left[ \left( \frac{1 + z_s}{1 + z_{\text{obs}}} \right)^{1.72} - 1 \right] \right\}, \end{aligned} \quad (14)$$

where  $X$  and  $Y$  are mass fractions of hydrogen and helium, respectively.

As we approximate the X-ray SED with a monochromatic frequency  $\nu_0$  and the bolometric X-ray luminosity  $L_0$  ( $\equiv \int_{X\text{-ray}} L_{\nu_s} d\nu_s$ ), Equation (8) can be simplified as:

$$\begin{aligned} L_{\nu_s, \text{Box}}(z_s) &= L_{0, \text{Box}}(z_s) \delta^D(\nu_s - \nu_0) \\ &= L_{0, \text{Box}}(z_s) \frac{1 + z_{\text{obs}}}{\nu} \delta^D \left( 1 + z_s - \frac{1 + z_{\text{obs}}}{\nu} \nu_0 \right), \end{aligned} \quad (15)$$

and thus using Equations (11) and (15),

$$J_{\nu}(z_{\text{obs}}) = \left( \frac{\nu}{\nu_0} \right)^{3/2} \frac{c(1 + z_{\text{obs}})^{3/2}}{4\pi\nu_0 H_0 \sqrt{\Omega_m}} \frac{L_{0, \text{Box}}(z_s)}{V_{\text{Box}}} \exp(-\tau_{\nu_{\text{obs}}}), \quad (16)$$

where  $1 + z_s = (\nu_0/\nu)(1 + z_{\text{obs}})$  is implied.

In practice, Equation (16) should be integrated in piecewise frequency intervals due to the time-discrete nature of the simulation. Especially for the contribution from the most recent past to the present because spatial fluctuation will be non-negligible, we calculate the fluctuating 3D X-ray background by adopting a scheme by Ahn et al. (2009). We locate the 3D field of X-ray luminosities frozen at the most recent past in the full box periodically and calculate the contribution at every location of the box by summing over the full contribution from all the X-ray sources but within the corresponding lookback time. Since this includes an out-of-box contribution, it will differ from the X-ray intensity distribution calculated from sources only inside the box at the observed redshift.

We plot the X-ray background intensities of monochromatic 1 keV and 3 keV X-ray photons as functions of distance to the simulation box center in Figure 10. The X-ray background intensities from higher-redshift sources are represented by their redshifted photon energies, which are all uniform in space except for the most recent contribution. We also plot the local X-ray intensities from our ray-tracing calculation for comparison. We also perform the calculations for the sub-keV X-rays. They show that the X-ray intensities from outside the simulation volume are negligible because most of their photons are absorbed locally.

It is interesting to understand the relative importance of the X-ray effects between the local sources and the X-ray background in different regions. Inside the Rarepeak, the X-ray intensities from local sources are strong and are at the same level as the X-ray background from nearby sources, whereas outside the Rarepeak, the X-ray background dominates. The background outside has an equivalent X-ray intensity at the same order of magnitude as the Rarepeak region, which has a very high Pop III stellar density. The X-ray background intensities at  $\sim 20$  comoving Mpc away from the source region are about 10 and 50 times higher than those from the Rarepeak region alone at redshifts  $z = 17.9$  and 15, respectively. Thus, for the X-ray feedback, the mean IGM should be mainly heated and ionized by the external X-ray background rather than by any local sources. In addition, as the external background resides in lower frequencies, its impact on heating and ionization of the IGM is boosted from the sheer value of X-ray intensity by a factor of  $\sim$

$(\nu/\nu_0)^{-3}$ .

The X-ray background from 1 keV photons and 3 keV photons is indeed quite different due to its differing mean free paths. For the 1 keV photons, the background is dominated by cosmological nearby sources because the X-ray radiation from sources at a distance of  $dz > 2$  is negligible. This is consistent with the fact that the mean free paths for the 1 keV X-ray photons are  $\sim$  a hundred comoving Mpc (more specifically  $\sim 4 \times 10^4 / (1+z)^2$  comoving Mpc). Therefore, the background from the 1 keV case is not building up from these early redshifts. At even higher energies, the mean free path for 3 keV photons is a few Gpc in the mean IGM, resulting in a non-negligible fraction of the radiation from  $z \lesssim 25$  propagating to  $z = 15$ . However, since the total X-ray radiation energy density is increasing during this period, the contributions from distant ( $\Delta z \gg 1$ ) sources are still much weaker than those from the nearby sources.

We show the evolution of averaged intensities of the total X-ray background from all cases in Figure 11, including an additional monochromatic X-ray of 770 eV, which is the mean photon energy from the assumed SED in Section 2.3. At  $z = 15$ , while the total X-ray luminosity from all sources in the simulation box is  $7.1 \times 10^{43}$  erg s $^{-1}$ , the mean X-ray intensity is ranging from  $5 \times 10^{-9}$  to  $3 \times 10^{-7}$  erg cm $^{-2}$  s $^{-1}$  sr $^{-1}$  for low to high energy photons. The background of 3 keV photon case is more than twice as high as the 1 keV case because of the large mean free path of the higher-energy photons, and the ratio of background at 3 keV and 1 keV shows little evolution from  $z = 25$  to  $z = 15$ . The average intensities for the sub-keV cases of the entire simulated box are much weaker because most of the radiation is confined inside the Rarepeak. The 300 eV background is about two orders of magnitude smaller than that of the 3 keV case. However, since their attenuation in the IGM is much stronger (as shown in Figure 8), their heating and ionizing effects may still be as important as the higher-energy background.

At even lower redshifts, X-rays from Pop III binaries likely grow slowly or even start to drop due to Pop III star formation being suppressed by metal enrichment<sup>7</sup>; the X-ray background of higher-energy photons, which survive from higher redshifts, should be more important at later times. However, since the heating and ionizing effects are much weaker for the high-energy photons as shown in the previous subsection, the effects of their background are still expected to be weak. We will study the long-term effects of X-ray background in the next subsection.

### 5.3. Effects of X-Ray Background on the IGM

We now estimate the heating and ionizing effects of our X-ray background model by applying our one-zone model to each cell in the  $512^3$  base grid from the full simulation, starting at  $z = 24$ . At each snapshot that is separated by  $\Delta z \sim 0.5$ , we fix the density distribution and allow the electron fraction  $x_e$  and temperature  $T$  to evolve according to the one-zone model and the

<sup>7</sup> Though the Pop III star formation rate at lower redshifts is still very uncertain, e.g., Crosby et al. (2013b) suggests that Pop III star formation continues on at a pretty steady rate until at least  $z = 10$ .

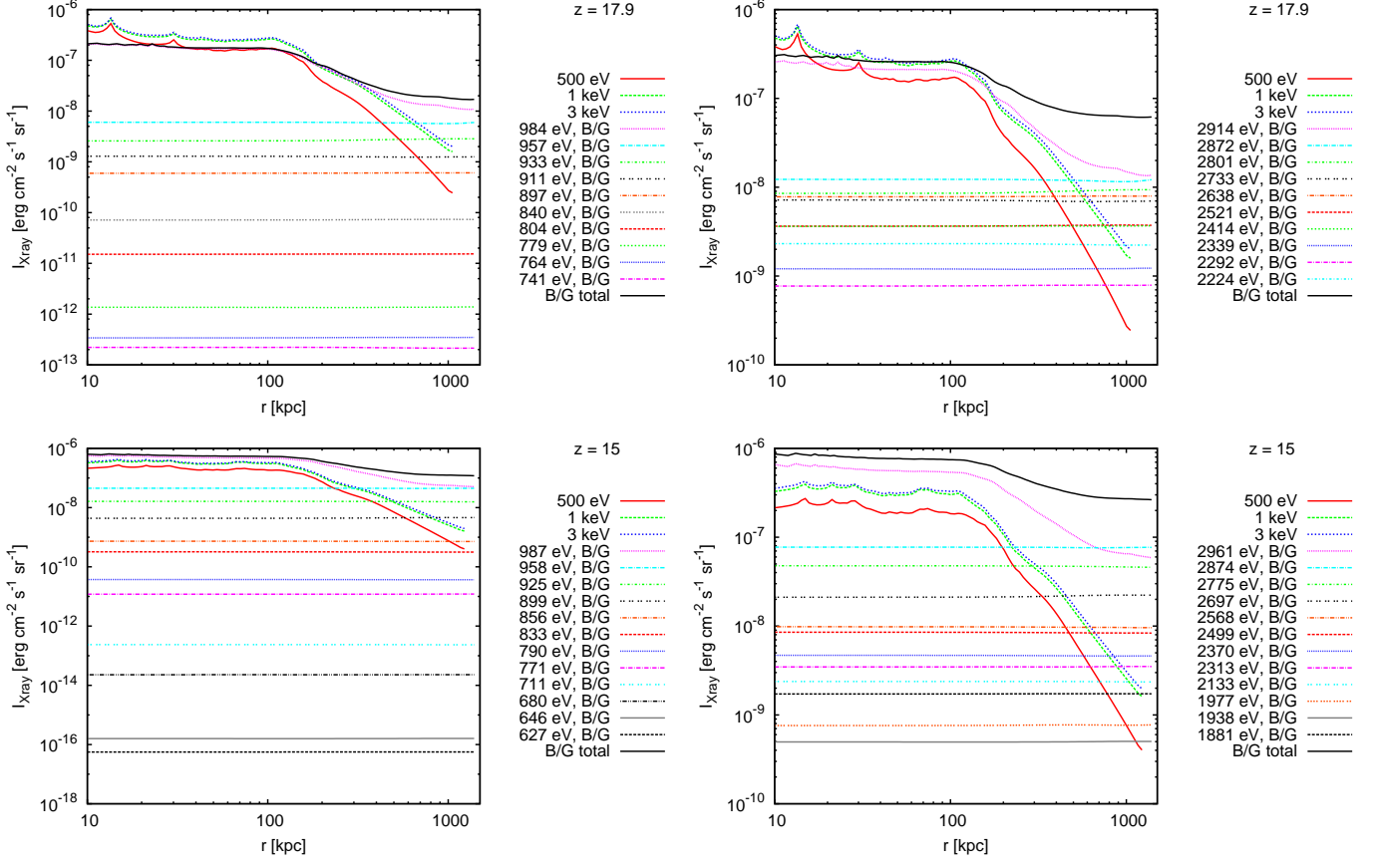


**Figure 10.** Distribution of X-ray intensities as function of the distance to the simulated volume center of 1 (left) and 3 (right) keV photons. The X-ray background from earlier redshifts is represented by the redshifted photon energy. For  $z = 15$ , background from some redshifts is omitted to make the figures simple. The X-ray intensities from ray tracing are plotted to show the relative importance between local sources and the background.

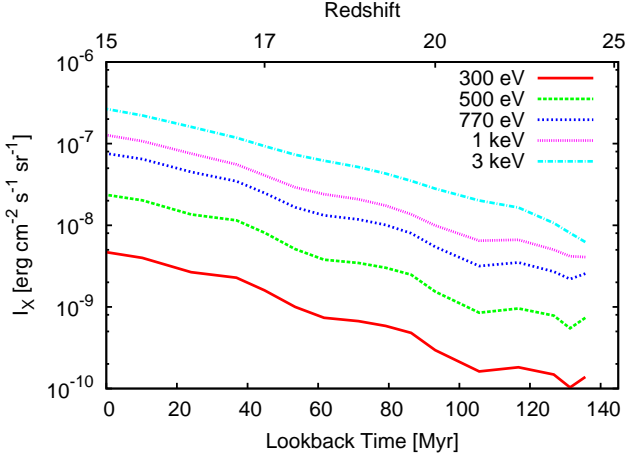


**Figure 11.** Evolution of the volume-weighted averaged intensity of the X-ray background of the entire simulated volume. The background from 3 keV photons is more than 2 times that from the 1 keV photons. The sub-keV X-rays in the simulation box are dominated by the Rarepeak sources and locally distributed, so their volumed-weighted intensities are much weaker than those of keV cases.

X-ray background intensity at the given redshift  $z_i$  and frequency. The X-ray heating and ionization by the redshifted photons with different energies and intensities are

calculated and summed at each timestep. We include the adiabatic expansion effect in calculating the temperature change. We then adjust the temperature and electron fraction in the next snapshot at redshifts  $z_i + \Delta z$  by  $\Delta T$  and  $\Delta x_e$ , respectively. This process is repeated until we reach the final redshift  $z = 15$  of the simulation. After this point, we fix the X-ray background and density distribution and continue the one-zone calculation for each cell to  $z = 6$ . We consider five cases with different photon energies of 300 eV, 500 eV, 770 eV, 1 keV, and 3 keV. As previously mentioned, the sub-keV cases locally heat and ionize the gas instead of adding to the background intensity. Although all of these calculations consider a monochromatic X-ray spectrum, nevertheless, we can obtain more realistic synthetic results by averaging the effects weighed by the luminosities based on the assumed SED in Section 2.3.

We first show the temperature and electron fraction volume-weighted averaged radial profiles at  $z = 15$  in Figure 12. We also plot the profiles from the original simulation with UV and other additional heating and cooling processes for comparison. Because the UV photoionization and photoheating are not considered in the one-zone model, the temperatures and ionization fractions at some radii inside Rarepeak are lower than the values from the original full simulation.

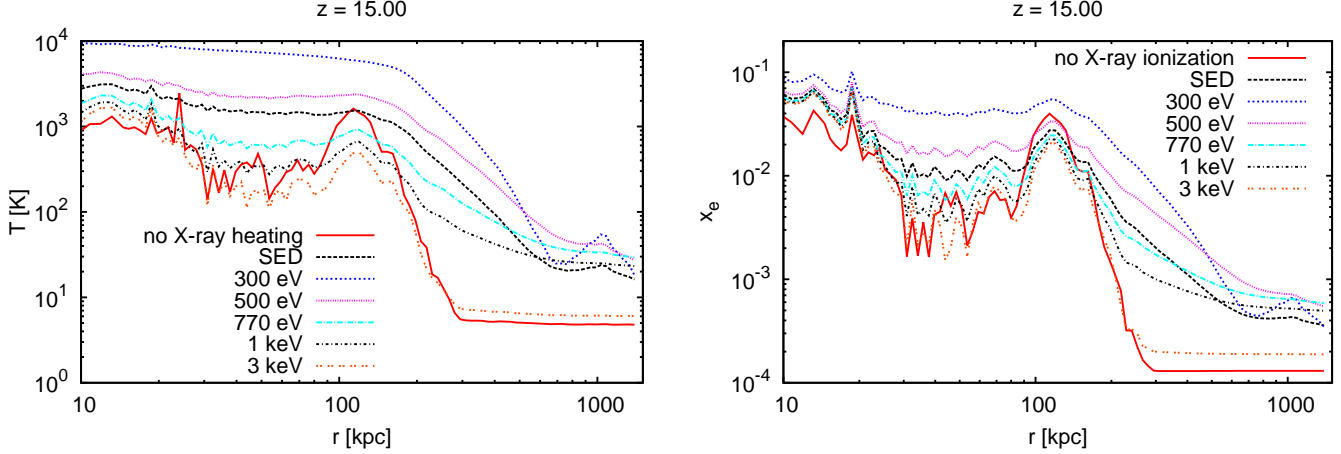


**Figure 12.** Volume-weighted averaged radial profiles at  $z=15$  of temperature (left) and electron fraction (right) of different X-ray photon energies.

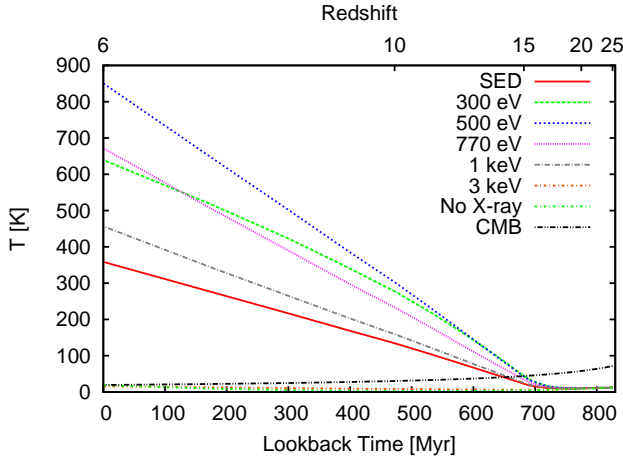


**Figure 13.** Evolution of the averaged IGM temperature to show the heating effect of the X-rays. We also plot the un-X-ray-heated temperature and the CMB temperature for reference.

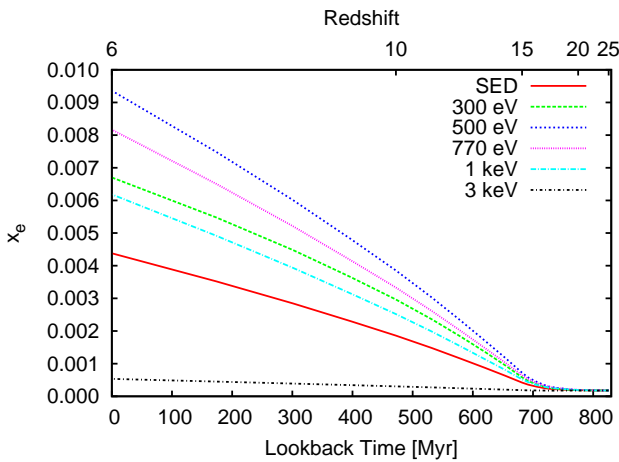


**Figure 14.** Evolution of the averaged electron fraction to show the ionization effect of the X-rays.

There are very different heating and ionization patterns for different photon energies.

- X-ray photoheating

1. Sub-keV Photons. The low-energy X-rays significantly heat both inside and outside the Rarepeak. Inside the Rarepeak, the X-ray heating pattern is much smoother than the individual H II regions created by UV photoheating. The heating is so strong that the temperatures of the 300 eV case are close to  $10^4$  K, which is limited by atomic hydrogen line cooling. Outside, the heating drops with a radius to close to the temperature of the 1 keV case at  $r > 1$  Mpc. The sub-keV cases are effected by outside (Rarepeak) sources significantly, then their radial profiles show bumps at a large radius.

2. KeV Photons. The heating effect of keV photons is very weak, both inside and outside the Rarepeak. There is no significant increase in temperature for 3 keV photons, while the heating of the 1 keV case is slightly more effective, resulting in  $\Delta T \sim 20$  K, close to those of sub-keV cases for a normal IGM at a large radius.

3. SED. The synthetic heating is similar to the 500 eV case, but weaker, inside and near Rarepeak, then it drops faster to even weaker than that of the 1 keV case at large distances ( $\sim 500$  proper kpc or 8 comoving Mpc).

- X-ray photoionization

The distribution of electron fraction is similar to the distribution of temperature. The electron fractions in all cases at  $\sim 1$  Mpc away from the center are smaller than  $10^{-3}$ . These ionization levels are not high enough to contribute to the optical depth to electron Thomson scattering of the CMB significantly ( $\delta\tau \ll 0.01$ ).

1. Sub-keV Photons. The highest electron fractions from the 300 eV case are just below 0.1 inside the Rarepeak. For the IGM outside of Rarepeak, the electron fraction of the 300 eV case is the highest at  $r \lesssim 500$  kpc, and then the 500 eV case has

the highest electron fraction. The effect of the 770 eV photons is closer to the 1 keV case than to the 500 eV case.

2. KeV Photons. The ionization effect of keV photons is very weak ( $\delta x_e < 10^{-3}$ ), both inside and outside the Rarepeak. The photoionization of 1 keV photons decreases slowly with radius due to their high escape fraction and then close to those of sub-keV cases at  $r > 1$  Mpc.

3. SED. The synthetic ionization is close to the 770 eV case, inside and near the Rarepeak (inside  $\sim 500$  proper kpc or 8 comoving Mpc radius), and then is even weaker than those of the 1 keV cases at large distances.

Figures 13 and 14 show the evolution of volume-weighted averaged temperature and electron fraction over the entire comoving  $(40 \text{ Mpc})^3$  simulated volume with results from the one-zone calculation of each cell, respectively. We exclude the central  $(8 \text{ comoving Mpc})^3$  region to obtain the mean values for a typical patch of the universe. For the temperature evolution, we also show the CMB temperature and the temperature from the hydrodynamical simulation. Star formation and feedback are not considered in the simulation after  $z = 15$  for computational reasons.

The results of this volumetric average are consistent with our one-zone calculation that uses a fixed initial conditions and X-ray flux, described in Section 5.1. This confirms that, at the same luminosity, the photon energy is the most important determinant in the heating and ionization history of the IGM.

- IGM temperature

Before  $z \sim 16$ , the X-ray background is still weak, and the heating of the IGM is not enough to compensate the decrease of temperature due to the adiabatic expansion. After that, the X-ray background is strong enough to increase the mean IGM temperature, which (except for the 3 keV case) passes the CMB temperature at redshifts just below 15, passes 100 K by  $z = 10$ , and then gradually increases to a range of 400 to 900 K at  $z = 6$ . Some regions, especially for the 300 eV case, are heated to over  $10^4$  K and then, are cooled by atomic hydrogen, resulting in a slowing down temperature growth.

1. Sub-keV Photons. Low-energy X-rays rapidly heat the IGM. The 300 eV photons significantly affect the regions near the sources, and the temperature growth slows approaching to  $\sim 640$  K because of a combination of the weak heating of the IGM outside of the Rarepeak and efficient radiative cooling near the Rarepeak. On the other hand, 500 and 770 eV X-rays continue to heat all the IGM of the simulated volume more effectively to higher than 850 and 670 K, respectively.

2. KeV Photons. The heating for the 1 keV radiation is much more pronounced than that of the 3 keV case, as its temperature reaches 450 K. For the 3 keV photons, though their intensity is more than twice stronger, the heating effect is so weak

that the IGM temperature only increases by a few Kelvin by  $z = 6$  when compared with the case without X-ray heating.

3. SED. The heating effect from the synthetic full spectrum is similar to that for the 1 keV case at large radii, and, accordingly, the mean temperature of the simulation volume is close to that of the 1 keV case. The mean IGM is heated to  $T \sim 360$  K at  $z = 6$ .

- IGM Electron Fraction

The evolution of electron fraction is simpler than the evolution of temperature because the equilibrium between photoionization and case B recombination is not yet reached in most of the volume for all cases.

1. Sub-keV Photons. The 500 eV X-rays are the most efficient in ionizing the entire volume because they can propagate farther away from their sources than lower-energy photons while having stronger interactions with the IGM than higher-energy photons. Our estimations show that, at  $z = 6$ , the maximal change in the volume-averaged electron fraction is  $\sim 0.01$ . The electron fractions are smaller for 300 and 770 eV photons, at 0.8% and just  $< 0.7\%$ , respectively. Though unlikely, if all of the X-ray radiation exists at  $\sim 500$  eV, its ionizations might contribute to the optical depth to the Thomson scattering.

2. KeV Photons. The X-ray background from 3 keV photons is inefficient in ionizing the IGM, only resulting in  $\Delta x_e \sim 10^{-3}$  by  $z = 6$ . The 1 keV X-rays photoionize the IGM moderately, to an electron fraction of  $x_e \sim 5 \times 10^{-4}$  at  $z \sim 15$  and  $\sim 6 \times 10^{-3}$  at  $z = 6$ .

3. SED. The mean IGM electron fraction from the synthetic full spectrum is only  $x_e \sim 2 \times 10^{-3}$  at  $z = 10$  and  $x_e < 5 \times 10^{-3}$  at  $z = 6$ , suggesting that ionizations from an X-ray background are a minor correction when calculating the optical depth due to Thomson scattering.

In summary, the IGM can be heated and ionized by the X-ray background from Pop III binaries. The photoionization effect is likely unimportant in direct observations, at least to the optical depth to Thomson scattering of the CMB, as the electron fraction might not be elevated over 0.005. However, this electron fraction could have some really substantial positive effects on  $H_2$  formation, and cause a general uptick in Pop III SFR elsewhere. On the other hand, the temperature of a large volume of the IGM may exceed 100 K by redshift  $z = 10$ . These heated regions of the IGM might be barely detectable by 21 cm SKA observations. The details of the mock 21 cm observations of Rarepeak and the surrounding area will be presented in a forthcoming paper (Ahn et al. 2014).

## 6. DISCUSSION AND CONCLUSIONS

In this paper, we utilize a self-consistent cosmological radiation hydrodynamic simulation of the formation of the first galaxies to study the luminosity, propagation and effects of X-rays generated by Pop III binaries. Using

the distribution and evolution of more than 13,000 Pop III stars and remnants in 3,000 halos in a survey volume of  $\sim 138$  comoving  $(\text{Mpc})^3$  from  $z = 30$  to  $z = 15$  and with a simplified Pop III XRB model, we estimate that there is an X-ray luminosity of  $\sim 10^{43}$  erg  $\text{s}^{-1}$  from the Rarepeak at  $z = 15$ , equating to a luminosity density of  $\sim 5 \times 10^{40}$  erg  $\text{s}^{-1}$  per comoving  $\text{Mpc}^3$ . We find that X-rays from Pop III binaries are much stronger than their UV ionizing radiation at pre-ionizing the universe, which dominate the photon budget in the early universe before galaxy formation becomes prevalent.

We study the impacts of these high-energy photons on the IGM in our simulated box of comoving  $(40 \text{ Mpc})^3$ . Due to the long mean free paths of X-ray photons (especially for keV photons) and the weak heating and photoionizing effects, radiation sources from cosmological distances and long integration times are needed for an accurate calculation. We combine three different methods—ray tracing, a one-zone model, and X-ray background modeling—for such a study in order to investigate the X-ray propagation, intensity distribution, and long-term effects on the IGM temperature and ionization. We first post-process the simulation with ray tracing to study the X-ray distribution through our simulated volume from the sources inside Rarepeak. Keeping the luminosity unchanged, we trace X-rays of 4 different monochromatic photon energies of 300 eV, 500 eV, 1 keV, and 3 keV. While sub-keV X-rays are significantly absorbed, higher-energy photons easily escape from halos and the high-density Rarepeak region. Thus, we conclude that keV radiation sources are likely the major contributor to the X-ray background. Our work also shows that local sources of X-rays do not have a significant impact on the typical IGM in a short period of time. Even the sub-keV X-rays, which are mostly absorbed locally, do not heat and ionize the gas fast and significantly with our calculated X-ray flux, suggesting that the ionization and thermal state of the IGM at high redshift is weakly dependent on the X-ray source population.

We estimate the evolution of the X-ray background using the X-ray intensity from our simulation by assuming some X-ray distribution outside the AMR refined region in our simulated box and using the mean IGM optical depth for hydrogen and helium. As suggested by our ray-tracing approach, only the keV photons can escape the galaxies and contribute meaningfully to the IGM X-ray background. For 1 keV photons, their mean free path is on the order of a hundred comoving Mpc, and only the photons from within  $\Delta z \sim 2$  contribute to the background. For higher-energy photons, their mean free path is on the order of 1 comoving Gpc, and the 3 keV background includes photons from nearly all radiation sources  $z > 15$ , resulting in the 3 keV X-ray background being more than double that of the 1 keV case.

We apply a one-zone model combining our X-ray background with the IGM properties from our simulation to estimate the heating and ionizing effects to the IGM everywhere inside our  $(40 \text{ comoving Mpc})^3$  box by the X-rays before reionization. As expected, they are very sensitive to the photon energies. Sub-keV X-rays, which only impact the nearby IGM and negligibly contribute to the background, can significantly heat and ionize the Rarepeak region and also have moderate heating and ionization effects on the nearby IGM. They heat the

Rarepeak region significantly (300 eV case even to  $10^4$  K), and may have important impacts on the ongoing star and galaxy formation. X-rays of  $\sim 1$  keV, which can escape the galaxies and Rarepeak region, also have moderate effects to the heat and ionize the IGM, and may contribute substantially to  $H_2$  formation in distant regions. The cool IGM might be heated to  $T \sim 100$  K at  $z < 10$  and ionized to nearly 0.5%. The interaction between higher-energy X-rays and the IGM is too weak to have a non-negligible effect on the thermal and ionization state of the IGM. When taking the spectrum energy distribution of the Pop III binary X-rays into account, the heating and ionization effects are weaker than the 1 keV case, but they are still substantial. The IGM heating might be detectable through 21 cm observations by SKA at  $z \lesssim 15$ . Since the temperature profiles are so different for different X-ray photon energies, 21 cm observations might possibly constrain the X-ray SED from Pop III binaries. The details on the possible 21-cm observations of these heated IGM will be reported in a forthcoming paper (Ahn et al. 2014). On the other hand, the increased ionization is so weak that it does not significantly contribute to the optical depth of the CMB to Thomson scattering. The ionization at these redshifts might then be dominated by the UV radiation from Pop II stars in low-mass metal cooling halos (Wise et al. 2014), which just form following the SN explosion of Pop III stars considered here.

We find that the sub-keV photons are most effective in locally heating and ionizing the IGM, and their effects on the IGM are much stronger than those by the X-ray background of higher-energy photons. Our simulated Rarepeak is a  $3.5\sigma$  density peak and the average distance between two similar peaks is only  $\sim 100$  comoving Mpc, suggesting that the IGM is more sensitive to lower-energy X-rays from nearby sources than to X-ray backgrounds of higher-energy photons.

The sources and amount of X-ray radiation in the early universe are under debate. Here, we only consider the possibility of Pop III binaries, but ignore other major sources, such as quasars, mini-quasars, and supernova remnants. However, our work suggests that the X-rays from Pop III binaries might dominate all other sources, at least at  $z > 10$ . It is generally thought that the two most important sources of X-rays in the universe are AGNs and XRBs (non-Pop III). The X-ray luminosity density inside Rarepeak<sup>8</sup> is  $\sim 5 \times 10^{40}$  erg  $\text{s}^{-1}$  per comoving  $\text{Mpc}^3$ , which is  $\sim 10$  times higher than that from normal XRBs at their peak at  $z \sim 3$ , and  $10^3$  times higher than that at  $z \sim 15$  (Fragos et al. 2013). X-rays from AGNs, estimated from both observations (Hasinger et al. 2005; Hopkins et al. 2007; Silverman et al. 2008; Aird et al. 2010) and semi-analytic models with N-body simulations (Croton et al. 2006), are only substantial at  $z < 6$ , and even at their peak at  $z \sim 3$ , their X-ray luminosity density is  $< 10^{40}$  erg  $\text{s}^{-1}$  comoving  $\text{Mpc}^{-3}$ .

However, since the Pop III initial mass function, binary fraction and evolution are not yet well constrained, our estimate of the X-ray luminosities and Pop III bi-

<sup>8</sup> Even in an unlikely scenario that Rarepeak contains the only X-ray sources inside the simulated volume, the X-ray luminosity density over the entire simulated box is still  $\sim 10^{38}$  erg  $\text{s}^{-1}$  per comoving  $\text{Mpc}^3$ .

nary SED are alone very uncertain, depending on the choice of model parameters, for instance, Pop III binary occurrence and BH mass. We might overestimate the X-ray output by assuming high Pop III binary occurrence and/or long binary lifetime by a factor of a few. However, even in such a case, Pop III binaries should still be the major sources of X-rays at high redshifts. On the other hand, we did not consider any X-rays from the later accretion to the BH after the companion of the binary dies, which could lead to an underestimation of the early X-ray background. However, we confirmed in the upper limit of the binaries accreting indefinitely that the Pop III contribution to the X-ray background is only a factor of a few higher. Our calculations show that even if the X-ray flux is 1–2 orders of magnitude stronger, it is still within the linear regime, and our results can be easily adjusted to another X-ray background that includes a more accurate model of Pop III binaries and other X-ray sources.

We have not considered the effects of relative streaming velocities ( $v_{vel} \sim 30 \text{ km s}^{-1}$  at  $z \sim 1100$ ) between baryons and dark matter that arise during recombination (Tseliakhovich & Hirata 2010). This phenomenon only suppresses Pop III star formation in the smallest mini-halos with  $M \leq 10^6 M_{\odot}$  (Tseliakhovich et al. 2011; Greif et al. 2011; Naoz et al. 2012; O’Leary & McQuinn 2012), which are not well resolved in our simulation, and should not significantly change our results. Additionally, after both Pop III and Pop II star formation gets going, the minimum halo mass in which Pop III star formation takes place rises to be substantially over  $10^6 M_{\odot}$  due to the LW background (Crosby et al. 2013b), thus making this effect quite unimportant. Xu et al. (2013) actually showed that the Pop III star formation in a few  $10^6 M_{\odot}$  halos in the high-density region of Rarepeak is already suppressed by the LW radiation by redshift  $z \sim 18$ . For studying an earlier phase of Pop III X-ray evolution, however, one may still need to increase mass resolution and include the relative streaming velocities simultaneously.

Currently, it is computationally unfeasible to execute a full radiation hydrodynamic simulation to  $z = 6$  in such a large high-density volume that resolves all Pop III-forming halos and calculates their formation rate. Without the exact evolution and distribution of Pop III formation at lower redshifts, we can only use a time-independent X-ray distribution to continue our calculations from  $z = 15$ . This assumption might not be much different than a self-consistent calculation of the X-ray background from Pop III binaries, though. As discussed in Xu et al. (2013), we expect that the Pop III formation will continue in the Rarepeak region but will be gradually suppressed. It is also likely that the Pop III formation in the other lower-density regions will become comparable to overdense regions like the Rarepeak. Recall that the halo mass function of this region at  $z = 15$  is similar to the  $z = 10$  halo mass function of an average patch of the universe. Thus, it is reasonable to expect that the X-rays from Pop III binaries will continue to much lower redshifts  $z \sim 10$  (also see Crosby et al. 2013b). We are currently running a similar simulation of an average region to lower redshifts. This, complementing the Rarepeak simulation, will provide a more complete understanding of the Pop III formation and X-ray background histories

before the end of the reionization.

We thank Jordan Mirocha for his comments on the paper. This research was supported by National Science Foundation (NSF) grant AST-1109243 to MLN. KA was supported by the NRF grant funded by the Korean government MEST (No. 2012R1A1A1014646). KA also acknowledges a very generous support from M. Norman for KA’s sabbatical visit to UCSD, where part of this work was performed as a collaboration between KA and Norman’s group members. JHW acknowledges support from NSF grants AST-1211626 and AST-1333360. BWO was supported in part by the MSU Institute for Cyber-Enabled Research. The simulation was performed using **Enzo** on the Kraken supercomputer operated for the Extreme Science and Engineering Discovery Environment (XSEDE) by the National Institute for Computational Science, ORNL with XRAC allocation MCA-TG98020N, and on the Blue Waters operated by the National Center for Supercomputing Applications (NCSA) with PRAC allocation support by the NSF (award number OCI-0832662). Data analysis was performed on the Gordon supercomputer operated for XSEDE by the San Diego Supercomputer Center and on the Blue Waters supercomputer. This research is part of the Blue Waters sustained-petascale computing project, which is supported by the NSF (award number ACI 1238993) and the state of Illinois. Blue Waters is a joint effort of the University of Illinois at Urbana-Champaign and its NCSA. This research has made use of NASAs Astrophysics Data System Bibliographic Services. The majority of the analysis and plots were done with **yt** (Turk et al. 2011). **Enzo** and **yt** are developed by a large number of independent researchers from numerous institutions around the world. Their commitment to open science has helped make this work possible.

## REFERENCES

- Abel, T., Anninos, P., Zhang, Y., & Norman, M. L. 1997, *New Astronomy*, 2, 181
- Abel, T., Bryan, G. L., & Norman, M. L. 2002, *Science*, 295, 93
- Ahn, K., Iliev, I. T., Shapiro, P. R., Mellema, G., Koda, J., & Mao, Y. 2012, *ApJ*, 756, L16
- Ahn, K., Shapiro, P. R., Iliev, I. T., Mellema, G., & Pen, U.-L. 2009, *ApJ*, 695, 1430
- Ahn, K., et al. 2014, *ArXiv e-prints* (arXiv:1405.2085)
- Aird, J., Nandra, K., Laird, E. S., Georgakakis, A., Ashby, M. L. N., Barmby, P., Coil, A. L., Huang, J.-S., Koekemoer, A. M., Steidel, C. C., & Willmer, C. N. A. 2010, *MNRAS*, 401, 2531
- Alvarez, M. A., Wise, J. H., & Abel, T. 2009, *ApJ*, 701, L133
- Becker, G. D., & Bolton, J. S. 2013, *MNRAS*, 436, 1023
- Bouwens, R. J., Illingworth, G. D., Oesch, P. A., Trenti, M., Labbé, I., Franx, M., Stiavelli, M., Carollo, C. M., van Dokkum, P., & Magee, D. 2012, *ApJ*, 752, L5
- Bromm, V., Coppi, P. S., & Larson, R. B. 2002, *ApJ*, 564, 23
- Bromm, V., Ferrara, A., Coppi, P. S., & Larson, R. B. 2001, *MNRAS*, 328, 969
- Bryan, G. L., Norman, M. L., O’Shea, B. W., Abel, T., Wise, J. H., Turk, M. J., Reynolds, D. R., Collins, D. C., Wang, P., Skillman, S. W., Smith, B., Harkness, R. P., Bordner, J., Kim, J.-h., Kuhlen, M., Xu, H., Goldbaum, N., Hummels, C., Kritsuk, A. G., Tasker, E., Skory, S., Simpson, C. M., Hahn, O., Oishi, J. S., So, G. C., Zhao, F., Cen, R., Li, Y., & The Enzo Collaboration. 2014, *ApJS*, 211, 19
- Chabrier, G. 2003, *PASP*, 115, 763
- Chen, P. F., Wise, J. H., Norman, M. L., & Xu, H. 2014, in preparation

- Crosby, B. D., O'Shea, B. W., Peruta, C., Beers, T. C., & Tumlinson, J. 2013a, ArXiv e-prints (arXiv:1312.0606)
- Crosby, B. D., O'Shea, B. W., Smith, B. D., Turk, M. J., & Hahn, O. 2013b, ApJ, 773, 108
- Croton, D. J., Springel, V., White, S. D. M., De Lucia, G., Frenk, C. S., Gao, L., Jenkins, A., Kauffmann, G., Navarro, J. F., & Yoshida, N. 2006, MNRAS, 365, 11
- Dijkstra, M., Haiman, Z., Rees, M. J., & Weinberg, D. H. 2004, ApJ, 601, 666
- Dopcke, G., Glover, S. C. O., Clark, P. C., & Klessen, R. S. 2013, ApJ, 766, 103
- Fan, X., Carilli, C. L., & Keating, B. 2006, ARA&A, 44, 415
- Fialkov, A., Barkana, R., Visbal, E., Tseliakhovich, D., & Hirata, C. M. 2013, MNRAS, 432, 2909
- Fialkov, A., Barkana, R., & Visbal, E. 2014, Nature, 506, 197
- Fragos, T., Lehmer, B. D., Naoz, S., Zezas, A., & Basu-Zych, A. 2013, ApJ, 776, L31
- Fryer, C. L. 1999, ApJ, 522, 413
- Furlanetto, S. R. 2006, MNRAS, 371, 867
- Gammie, C. F. 1999, ApJ, 522, L57
- Gnedin, N. Y. 2000, ApJ, 542, 535
- Gnedin, N. Y., & Ostriker, J. P. 1997, ApJ, 486, 581
- Gómez, F. A., Coleman-Smith, C. E., O'Shea, B. W., Tumlinson, J., & Wolpert, R. L. 2012, ApJ, 760, 112
- Greif, T. H., Bromm, V., Clark, P. C., Glover, S. C. O., Smith, R. J., Klessen, R. S., Yoshida, N., & Springel, V. 2012, MNRAS, 424, 399
- Greif, T. H., Glover, S. C. O., Bromm, V., & Klessen, R. S. 2010, ApJ, 716, 510
- Greif, T. H., White, S. D. M., Klessen, R. S., & Springel, V. 2011, ApJ, 736, 147
- Haardt, F., & Madau, P. 2012, ApJ, 746, 125
- Hahn, O., & Abel, T. 2011, MNRAS, 415, 2101
- Haiman, Z. 2011, Nature, 472, 47
- Haiman, Z., Abel, T., & Rees, M. J. 2000, ApJ, 534, 11
- Haiman, Z., & Bryan, G. L. 2006, ApJ, 650, 7
- Hasinger, G., Miyaji, T., & Schmidt, M. 2005, A&A, 441, 417
- Heger, A., Fryer, C. L., Woosley, S. E., Langer, N., & Hartmann, D. H. 2003, ApJ, 591, 288
- Hopkins, P. F., Richards, G. T., & Hernquist, L. 2007, ApJ, 654, 731
- Janev, R. K., Langer, W. D., & Evans, K. 1987, Elementary processes in Hydrogen-Helium plasmas - Cross sections and reaction rate coefficients
- Jeon, M., Pawlik, A. H., Bromm, V., & Milosavljevic, M. 2013, ArXiv e-prints (arXiv:1310.7944)
- Karlsson, T., Johnson, J. L., & Bromm, V. 2008, ApJ, 679, 6
- Komatsu, E., Smith, K. M., Dunkley, J., Bennett, C. L., Gold, B., Hinshaw, G., Jarosik, N., Larson, D., Nolte, M. R., Page, L., Spergel, D. N., Halpern, M., Hill, R. S., Kogut, A., Limon, M., Meyer, S. S., Odegard, N., Tucker, G. S., Weiland, J. L., Wollack, E., & Wright, E. L. 2011, ApJS, 192, 18
- Komiya, Y., Habe, A., Suda, T., & Fujimoto, M. Y. 2010, ApJ, 717, 542
- Kuhlen, M., & Madau, P. 2005, MNRAS, 363, 1069
- Larson, R. B. 2005, MNRAS, 359, 211
- Machacek, M. E., Bryan, G. L., & Abel, T. 2001, ApJ, 548, 509
- Maio, U., Ciardi, B., Dolag, K., Tornatore, L., & Khochfar, S. 2010, MNRAS, 407, 1003
- Makishima, K., Kubota, A., Mizuno, T., Ohnishi, T., Tashiro, M., Aruga, Y., Asai, K., Dotani, T., Mitsuda, K., Ueda, Y., Uno, S., Yamaoka, K., Ebisawa, K., Kohmura, Y., & Okada, K. 2000, ApJ, 535, 632
- Meece, G. R., Smith, B. D., & O'Shea, B. W. 2014, ApJ, 783, 75
- Mesinger, A., Ferrara, A., & Spiegel, D. S. 2013, MNRAS, 431, 621
- Mirabel, I. F., Dijkstra, M., Laurent, P., Loeb, A., & Pritchard, J. R. 2011, A&A, 528, A149
- Mitsuda, K., Inoue, H., Koyama, K., Makishima, K., Matsuoka, M., Ogawara, Y., Suzuki, K., Tanaka, Y., Shibazaki, N., & Hirano, T. 1984, PASJ, 36, 741
- Muratov, A. L., Gnedin, O. Y., Gnedin, N. Y., & Zemp, M. 2013a, ApJ, 772, 106
- . 2013b, ApJ, 773, 19
- Naoz, S., Yoshida, N., & Gnedin, N. Y. 2012, ApJ, 747, 128
- Oh, S. P. 2001, ApJ, 553, 499
- O'Leary, R. M., & McQuinn, M. 2012, ApJ, 760, 4
- Omukai, K. 2000, ApJ, 534, 809
- Omukai, K., Hosokawa, T., & Yoshida, N. 2010, ApJ, 722, 1793
- Omukai, K., Tsuribe, T., Schneider, R., & Ferrara, A. 2005, ApJ, 626, 627
- O'Shea, B. W., & Norman, M. L. 2007, ApJ, 654, 66
- . 2008, ApJ, 673, 14
- Osterbrock, D. E. 1989, Astrophysics of gaseous nebulae and active galactic nuclei, ed. Osterbrock, D. E.
- Ostriker, J. P., & Gnedin, N. Y. 1996, ApJ, 472, L63
- Parsons, A. R., Liu, A., Aguirre, J. E., et al. 2013, ArXiv e-prints (arXiv:1304.4991)
- Planck Collaboration, Ade, P. A. R., Aghanim, N., Armitage-Caplan, C., Arnaud, M., Ashdown, M., Atrio-Barandela, F., Aumont, J., Baccigalupi, C., Banday, A. J., & et al. 2013, ArXiv e-prints (arXiv:1303.5076)
- Power, C., Wynn, G. A., Combet, C., & Wilkinson, M. I. 2009, MNRAS, 395, 1146
- Pritchard, J. R., & Furlanetto, S. R. 2007, MNRAS, 376, 1680
- Ricotti, M., Gnedin, N. Y., & Shull, J. M. 2001, ApJ, 560, 580
- . 2002a, ApJ, 575, 33
- . 2002b, ApJ, 575, 49
- . 2008, ApJ, 685, 21
- Ricotti, M., & Ostriker, J. P. 2004, MNRAS, 352, 547
- Ricotti, M., Ostriker, J. P., & Gnedin, N. Y. 2005, MNRAS, 357, 207
- Salvadori, S., Schneider, R., & Ferrara, A. 2007, MNRAS, 381, 647
- Scannapieco, E., Schneider, R., & Ferrara, A. 2003, ApJ, 589, 35
- Schaerer, D. 2002, A&A, 382, 28
- Schneider, R., & Omukai, K. 2010, MNRAS, 402, 429
- Schneider, R., Omukai, K., Inoue, A. K., & Ferrara, A. 2006, MNRAS, 369, 1437
- Shull, J. M., & van Steenberg, M. E. 1985, ApJ, 298, 268
- Silverman, J. D., Green, P. J., Barkhouse, W. A., Kim, D.-W., Kim, M., Wilkes, B. J., Cameron, R. A., Hasinger, G., Jannuzi, B. T., Smith, M. G., Smith, P. S., & Tananbaum, H. 2008, ApJ, 679, 118
- Smith, B. D., Turk, M. J., Sigurdsson, S., O'Shea, B. W., & Norman, M. L. 2009, ApJ, 691, 441
- Sobacchi, E., & Mesinger, A. 2013, MNRAS, 432, 3340
- Stacy, A., & Bromm, V. 2013, MNRAS, 433, 1094
- Stacy, A., Greif, T. H., & Bromm, V. 2010, MNRAS, 403, 45
- Sutherland, R. S., & Dopita, M. A. 1993, ApJS, 88, 253
- Tanaka, T., Perna, R., & Haiman, Z. 2012, MNRAS, 425, 2974
- Thorne, K. S. 1974, ApJ, 191, 507
- Tornatore, L., Ferrara, A., & Schneider, R. 2007, MNRAS, 382, 945
- Trenti, M., Stiavelli, M., & Shull, J. M. 2009, ApJ, 700, 1672
- Tseliakhovich, D., Barkana, R., & Hirata, C. M. 2011, MNRAS, 418, 906
- Tseliakhovich, D., & Hirata, C. 2010, Phys. Rev. D, 82, 083520
- Tumlinson, J. 2006, ApJ, 641, 1
- Turk, M. J., Abel, T., & O'Shea, B. 2009, Science, 325, 601
- Turk, M. J., Smith, B. D., Oishi, J. S., Skory, S., Skillman, S. W., Abel, T., & Norman, M. L. 2011, ApJS, 192, 9
- Venkatesan, A., Giroux, M. L., & Shull, J. M. 2001, ApJ, 563, 1
- Whalen, D., O'Shea, B. W., Smidt, J., & Norman, M. L. 2008a, ApJ, 679, 925
- Whalen, D., van Veelen, B., O'Shea, B. W., & Norman, M. L. 2008b, ApJ, 682, 49
- Willott, C. J., Delorme, P., Reylé, C., Albert, L., Bergeron, J., Crampton, D., Delfosse, X., Forveille, T., Hutchings, J. B., McLure, R. J., Omont, A., & Schade, D. 2010, AJ, 139, 906
- Wise, J. H., & Abel, T. 2005, ApJ, 629, 615
- . 2007, ApJ, 671, 1559
- . 2008, ApJ, 685, 40
- . 2011, MNRAS, 414, 3458
- Wise, J. H., Abel, T., Turk, M. J., Norman, M. L., & Smith, B. D. 2012a, MNRAS, 427, 311
- Wise, J. H., Demchenko, V. G., Halicek, M. T., Norman, M. L., Turk, M. J., Abel, T., & Smith, B. D. 2014, MNRAS, 442, 2560
- Wise, J. H., Turk, M. J., Norman, M. L., & Abel, T. 2012b, ApJ, 745, 50
- Xu, H., Wise, J. H., & Norman, M. L. 2013, ApJ, 773, 83
- Yoshida, N., Abel, T., Hernquist, L., & Sugiyama, N. 2003, ApJ, 592, 645
- Yoshida, N., Bromm, V., & Hernquist, L. 2004, ApJ, 605, 579

Zahn, O., Reichardt, C. L., Shaw, L., Lidz, A., Aird, K. A.,  
Benson, B. A., Bleem, L. E., Carlstrom, J. E., Chang, C. L.,  
Cho, H. M., Crawford, T. M., Crites, A. T., de Haan, T.,  
Dobbs, M. A., Doré, O., Dudley, J., George, E. M., Halverson,  
N. W., Holder, G. P., Holzappel, W. L., Hoover, S., Hou, Z.,  
Hrubes, J. D., Joy, M., Keisler, R., Knox, L., Lee, A. T.,  
Leitch, E. M., Lueker, M., Luong-Van, D., McMahon, J. J.,  
Mehl, J., Meyer, S. S., Millea, M., Mohr, J. J., Montroy, T. E.,  
Natoli, T., Padin, S., Plagge, T., Pryke, C., Ruhl, J. E.,  
Schaffer, K. K., Shirokoff, E., Spieler, H. G., Staniszewski, Z.,  
Stark, A. A., Story, K., van Engelen, A., Vanderlinde, K.,  
Vieira, J. D., & Williamson, R. 2012, ApJ, 756, 65